Author's Accepted Manuscript

Latitudinal distributions of particulate carbon export across the North Western Atlantic Ocean

Viena Puigcorbé, Montserrat Roca-Martí, Pere Masqué, Claudia Benitez-Nelson, Michiel Rutgers van der Loeff, Astrid Bracher, Sebastien Moreau

DEEP-SEA RESEARCH

PART I

Oceanographic Research Papers

www.elsevier.com/locate/dsr

www.elsevier.com

Cite this article as: Viena Puigcorbé, Montserrat Roca-Martí, Pere Masqué, Claudia Benitez-Nelson, Michiel Rutgers van der Loeff, Astrid Bracher and Sebastien Moreau, Latitudinal distributions of particulate carbon export across the North Western Atlantic Ocean, *Deep-Sea Research Part I,* http://dx.doi.org/10.1016/j.dsr.2017.08.016

Latitudinal distributions of particulate carbon export-across the North Western Atlantic Ocean

Viena Puigcorbé[1,2], Montserrat Roca-Martí[1], Pere Masqué[1,2,3], Claudia Benitez-Nelson[4], Michiel Rutgers van der Loeff[5], Astrid Bracher[5,6], Sebastien Moreau[7]

[1]Institut de Ciència i Tecnologia Ambientals & Departament de Física, Universitat Autònoma de Barcelona, Bellaterra, Spain

[2]School of Natural Sciences & Centre for Marine Ecosystems Research, Edith Cowan University, School of Science, Joondalup, WA, Australia

[3]Oceans Institute & School of Physics. The University of Western Australia. 35 Stirling Highway. Crawley, WA, Australia

[4]School of the Earth, Ocean & Environment, University of South Carolina, Columbia, SC, USA

[5]Alfred Wegener Institute Helmholtz Center for Polar and Marine Research, Bremerhaven, Germany

[6] Institute of Environmental Physics, University of Bremen, Bremen, Germany

[7] Institute for Marine and Antarctic Studies, University of Tasmania, Hobart, Australia

Abstract

[234]Th-derived carbon export fluxes were measured in the Atlantic Ocean under the GEOTRACES framework to evaluate basin-scale export variability. Here, we present the results from the northern half of the GA02 transect, spanning from the equator to 64°N. As a result of limited site-specific $C/^{234}Th$ ratio measurements, we further combined our data with previous work to develop a basin wide $C/^{234}Th$ ratio depth curve. While the magnitude of organic carbon fluxes varied depending on the $C/^{234}Th$ ratio used, latitudinal trends were similar, with sizeable and variable organic carbon export fluxes occurring at high latitudes and low to negligible fluxes occurring in oligotrophic waters. Our results agree with previous studies, except at the boundaries between domains, where fluxes were relatively enhanced.

Three different models were used to obtain satellite-derived net primary production (NPP). In general, NPP estimates had similar trends along the transect, but there were significant differences in the absolute magnitude depending on the model used. Nevertheless, organic carbon export efficiencies were generally < 25%, with the exception of a few stations located in the transition area between the riverine and the oligotrophic domains and between the oligotrophic and the temperate domains. Satellite-derived organic carbon export models from Dunne et al. (2005) (D05), Laws et al. (2011) (L11) and Henson et al. (2011) (H11) were also compared to our [234]Th-derived carbon exports fluxes. D05 and L11 provided estimates closest to values obtained with the [234]Th approach (within a 3-fold difference), but with no clear trends. The H11 model, on the other hand, consistently provided lower export estimates.

The large increase in export data in the Atlantic Ocean derived from the GEOTRACES Program, combined with satellite observations and modeling efforts continue to improve the estimates of carbon export in this ocean basin and therefore reduce uncertainty in the global carbon budget. However, our results also suggest that tuning export models and including biological parameters at a regional scale is necessary for improving satellite-modeling efforts and providing export estimates that are more representative of *in situ* observations.

1. INTRODUCTION

The biogeochemical cycling of carbon and major nutrients is strongly influenced by particle cycling and export (Honjo et al., 2008). Carbon dioxide fixation by phytoplankton and the subsequent downward particle flux of biogenic carbon, a process often referred to as the "biological pump" (Volk and Hoffert, 1985), is a key component in the global carbon cycle. Yet the understanding of the magnitude and variability of this flux over temporal and spatial scales remains limited (Britten and Primeau, 2016; Burd et al., 2010). As a consequence, global-scale models of ocean carbon export vary widely, ranging from ~ 5 to 13 Gt C y^{-1} (Henson et al., 2011; Laws et al., 2011; Siegel et al., 2014). This uncertainty highlights the need for continuing *in situ* carbon export field sampling

over large geographical provinces and across seasonal timescales (Britten and Primeau, 2016; Siegel et al., 2016).

Thorium-234 has been widely used as a tracer to estimate particle fluxes (e.g., Coale and Bruland, 1985; Cochran and Masqué, 2003) and, to a lesser extent, remineralization in the upper ocean (Maiti et al., 2010; Savoye et al., 2004). The estimation of particulate organic carbon (POC) fluxes has been the most significant application of the ^{234}Th:^{238}U disequilibrium method, since the ^{234}Th half-life (24.1 days) makes it a suitable tracer to examine seasonal changes in POC production and export (see review by Waples et al., 2006). However, POC export and remineralization processes also influence other elements, such as trace metals essential for phytoplankton growth and biological functioning (e.g., Fe, Cd or Co) or particle-reactive elements (e.g., Pb or Al) and compounds (e.g., polychlorinated biphenyls, PCBs) that are scavenged from the surface ocean and adsorbed onto settling particles (Dulaquais et al., 2014; Gustafsson et al., 1997a, 1997b; Weinstein and Moran, 2005). Thus, the use of ^{234}Th as a particle tracer provides essential information for constraining processes such as particle dynamics and trace element cycling and their distribution in the ocean.

GEOTRACES is an ideal platform to examine particle flux across large-scale latitudinal and longitudinal gradients. As part of the Dutch GEOTRACES program, the GA02 section was sampled in 2010-2011. This section covered more than 17,000 km at high spatial resolution (usually < 2º latitude, ~150 km) and spanned a diversity of biogeochemical regions, such as deep-water formation zones, subtropical gyres, oligotrophic seas, waters with significant dust inputs, and areas influenced by riverine outflows. Here, we discuss ^{234}Th and ^{234}Th-derived organic carbon export fluxes obtained in the northern half of that section, from the Irminger Sea, southeast of Greenland, to the equator (Figure 1). The southern half of the transect is presented in Owens et al. (2015). We describe regional export variability in the North Western Atlantic Ocean and the results are discussed with regards to various regional processes. We also present a compilation of POC export estimates (hereafter C export) from previous open ocean studies using ^{234}Th:^{238}U disequilibria in the

North Atlantic Ocean, provide estimates of C export efficiencies, and compare our [234]Th-derived C export fluxes with different satellite-based export models.

This work contributes to the growing database of [234]Th-derived export measurements by providing data across a wide variety of biogeochemical regions that can be used to not only constrain C export estimates at an oceanic scale, but also to answer questions regarding particle cycling, export, and remineralization rates of trace elements in the North Atlantic Ocean.

2. MATERIALS AND METHODS

2.1 Total [234]Th

A total of 33 stations were sampled (n = 344 samples) for total [234]Th activities (dpm L^{-1}) from 64ºN to the equator. Samples were collected during two consecutive cruises: 64PE319 (28 April to 25 May) and 64PE321 (11 June to 8 July), on board the R/V *Pelagia* in 2010 (Figure 1, Table S1). Total [234]Th activities were measured from 4 L of seawater collected at a minimum of 12 depths over the upper 1000 m. Samples were processed following the MnO_2 co-precipitation technique (Buesseler et al., 2001) and counted on board using a gas flow proportional low-level RISØ beta counter (uncertainty from counting statistics < 3%). Samples were recounted > 6 months later to determine background activities before processing for chemical recoveries using ICP-MS. Relative efficiency calibration of the RISØ detectors was carried out at the beginning and at the end of the cruise using [238]U standards to ensure stability of the measurements. Five replicates of deep samples (≥ 1750 m) were collected at selected stations of each cruise for calibration purposes, obtaining a [234]Th:[238]U ratio of 1.02 ± 0.03. The efficiency calibration of the RISO counters for both water and particulate samples was also confirmed through the GEOTRACES intercalibration program (Maiti et al., 2012).

The determination of the Th recovery was conducted using the method described in Pike et al. (2005), modified to remove the column purification step (see Puigcorbé et al., 2017 for details). The

average recovery of [230]Th was $88 \pm 13\%$ (n = 335). Uranium-238 activities were calculated from salinity using the relationship established by Owens et al. (2011). The U-salinity relationship was further confirmed by direct measurement of [238]U concentrations (Casacuberta et al., 2014) in samples collected during the same expeditions (n = 15). [234]Th activities were corrected for ingrowth and decay to the date and time of sample collection. Uncertainties for [234]Th activities were obtained by propagating errors associated with counting, detector calibration, [238]U activities, and background corrections. Combined, they averaged $5 \pm 1\%$ (n = 344) and were always $\leq 10\%$. [234]Th and [238]U activities along the GA02 transect are available online (British Oceanographic Data Centre, http://www.bodc.ac.uk/geotraces/data/idp2014/) and are part of the GEOTRACES Intermediate Data Product 2014 (Mawji et al., 2015).

2.2 Particulate [234]Th and particulate organic carbon

Samples for particulate [234]Th and organic C were collected at 11 stations using *in situ* McLane and Challenger filtration pumps (ISP) deployed at 100 m (see Figure 1). Pumping times lasted about 2.5 h and the volume filtered ranged from 1800 to 2200 L. Particles were collected using a 53 μm mesh Nitex screen. The material was washed off the screen with 0.2 μm-filtered seawater and an aliquot equivalent to 100 - 900 L was filtered with positive pressure (< 0.3 bar) onto a 0.45 μm pore-size silver filter (Millipore). Particulate [234]Th was measured on board and recounted for background activities > 6 months after collection, similar to the water samples. POC concentrations were determined back in the laboratory with an Eurovector C/N Element analyzer according to the JGOFS protocols (Knap et al., 1996), after being treated with 0.1 M HCl solution to remove carbonate.

2.3 Satellite data

Primary productivity

Carbon export rates are commonly compared to the productivity of the regional biological regime. Three commonly applied approaches have been used to obtain net primary productivity rates (NPP) from satellite data (Table S1). These models differ in how they address the physiological complexity of phytoplankton productivity. As such, each have their own strengths and weaknesses, which become most apparent when comparing them across different temporal and spatial scales, particularly at high latitudes (Palevsky et al., 2016). The lack of consensus as to which model is the most accurate in representing *in situ* NPP at a basin-wide scale remains an ongoing research effort (Kahru, 2017).

In the first approach, NPP rates in g C m^{-2} day^{-1} were taken from the GlobColour OSS2015 demonstration products as monthly mean values collocated to the sampled stations with 25-km resolution (the product is not available for the timing of the sampled stations at higher temporal or spatial resolution). As described in the GlobColour product user guide (GlobColour, 2015), NPP was calculated from the GlobColour level-3 chlorophyll-a (Chl-a) concentration, photosynthetic available radiation (PAR) and sea surface temperature (SST) following the method of Antoine and Morel (1996) (A&M96). This model assesses the primary production from the Chl-a concentration in a conceptually similar way to an absorption-based model. The A&M96 a model, based on Morel, (1991)*,* is formulated using chlorophyll specific wavelength-resolved absorption and quantum yield. Temperature dependence is given by the parameterization of the maximum photosynthetic yield, which follows Eppley (1972). Mean photo-physiological parameters are from Morel et al. (1996). The model is run in its "satellite" version (Antoine et al., 1996), where NPP is the product of integral biomass (chlorophyll), the daily irradiance, and the cross section of algae for photosynthesis per unit of areal chlorophyll biomass.

NPP was also obtained from the Ocean Productivity website at Oregon State University (http://www.science.oregonstate.edu/ocean.productivity/) with a 9-km spatial resolution and 8 day temporal resolution data from MODIS and SeaWiFS satellites. We used both the Vertically Generalized Production Model (VGMP; Behrenfeld and Falkowski, 1997a) and the Carbon-based

Production Model (CbPM; Behrenfeld et al., 2005; Westberry et al., 2008). VGPM is a "chlorophyll-based" model: it estimates NPP from satellite Chl-a, available light and photosynthetic efficiency, and the empirically-determined relationship between carbon assimilation and SST. The VGPM model is simpler than the A&M96 model since, in general, the A&M06 model accounts for the difference of the phytoplankton distribution in the vertical profile and its spectral absorption properties, while these are assumed constant in the VGPM approach (Behrenfeld and Falkowski, 1997b).

CbPM is a carbon-based model where NPP is the product of carbon biomass and growth rate. This model uses remote sensing retrievals of particulate scattering coefficients to estimate phytoplankton carbon concentration, thus replacing chlorophyll as the metric of biomass (Behrenfeld et al., 2005). It further accounts for nutrient- and light-dependent changes in phytoplankton physiology with depth (Westberry et al., 2008). Nine km resolution SST and satellite-derived Chl-a were obtained from the OceanColor Data website (http://oceandata.sci.gsfc.nasa.gov). The depth of the euphotic zone (Z_{eu}) was calculated from Chl-a following Morel and Berthon (1989) (Table S1). Weekly NPP, SST and Z_{eu} at 9-km resolution were calculated for all the sampling stations by integrating ~ 4 weeks (32 days) prior the sampling in order to compare with the integration time of ^{234}Th (mean life ~ 35 days). Satellite-derived Chl-a values integrated over the 8 days prior to sampling as well as monthly averages were comparable to the *in situ* fluorescence values (expressed in mg Chl-a m^{-2}) measured during the expeditions ($p = 0.15$ and $p = 0.055$, respectively).

Satellite-derived organic carbon export models

Organic carbon export was estimated from three widely-used global models, using satellite-derived SST, NPP and Z_{eu} from above: i) Dunne et al. (2005) (D05); ii) Laws et al. (2011) (L11); and iii) Henson et al. (2011) (H11). The D05 model, which is an empirical model based on a compilation of export data obtained through a variety of methodologies, provides export estimates using SST and NPP as predictor variables, and is computed as:

$$\text{Export (D05)} = \text{NPP} \times [\ -0.0101°C^{-1} \times \text{SST} + 0.0582 \times \ln(\text{NPP}/Z_{eu}) + 0.419]$$

The L11 model is a steady-state food web model with a negative relationship between export and temperature and a curvilinear correlation between export and NPP:

$$\text{Export (L11)} = \text{NPP} \times 0.04756 \ (0.78 - 0.43 \ \text{SST} / 30) \ \text{NPP}^{0.307}$$

The H11 model is based on an exponential relationship between [234]Th-derived export below 100 m and SST and is computed as:

$$\text{Export (H11)} = \text{NPP} \times 0.23 \times \text{EXP}(-0.08 \times \text{SST})$$

2.4 Complementary data

Oceanographic data (temperature, salinity, attenuation coefficient, fluorescence and dissolved oxygen) were obtained from sensors attached to sampling rosette, which included a Seabird SBE9+ Underwater Unit with a SBE4 conductivity sensor ($\pm$ 0.3 mS m^{-1}), a SBE3+ thermometer ($\pm$ 0.001°C), a Chelsea Aquatracka MKIII fluorometer ($\pm$ 0.2 µg L^{-1}), a Wetlabs C-Star transmissometer ($\pm$ 0.02%FS °C^{-1}) and a SBE43 dissolved oxygen sensor ($\pm$ 2%). Nutrient concentrations were determined colorimetrically according to the methods described by Grasshoff et al. (1983). Analyses were performed on board using a Seal Analytical QuAAtro Autoanalyser as detailed in the cruise reports (64PE319: Gerringa, 2010; 64PE321: Rijkenberg, 2010).

3. RESULTS

3.1 Hydrography

The northern GA-02 section covered the Atlantic Ocean from the Irminger Sea to the equator along the deep basins of the western Atlantic Ocean (Figure 1). A detailed hydrographical description of the complete GA-02 section can be found in van Aken (2011). Briefly, the subarctic gyre, with cold water temperatures (< 10ºC) and low salinities (< 35), was separated from the warm and saltier subtropical gyre by a front located at ~ 50ºN. Labrador Sea Water (LSW) was found in the upper 1000 m between 50ºN and 64ºN, where high oxygen concentrations (> 300 µmol kg^{-3}) were

measured down to 1000 m. Surface waters were characterized by high nitrate and phosphate concentrations (> 10 μM NO_3^-, > 0.8 μM PO_4^{3-}), indicating a weak or absent seasonal thermocline. Across the subtropical gyre, temperature and salinity increased towards the south, with a clearly stratified water column, nutrients became increasingly depleted in surface waters (~ 25 m) and 1 μM NO_3^- and 0.1 μM PO_4^{3-} isoclines deepened, reaching depths of ~ 250 m at ~ 25ºN. Within this oligotrophic area, the influence of the Amazon River plume was noticeable in the upper layer (~ 30 m) between 11ºN and 18ºN, as reflected by low salinity (< 34) and higher silicate concentrations, as high as 8 μM at 10 m. Fluorescence and beam attenuation also reflected the intrusion of the river plume, as well as high Chl-a concentrations derived from satellite data (Figure 1). Between the equator and 10ºN the water column remained strongly stratified, with the nutricline being slightly shallower (75 - 100 m). The influence of the Amazon River plume was also observed at ~ 4ºN, with low salinity (< 34.5) and high silicate concentrations (~ 8.0 μM), although the signal was weaker compared to the one observed further north. The high nutrient concentrations at depth, between 600 and 1200 m, were coincident with the oxygen minimum zone and Antarctic Intermediate Water (AAIW). These main hydrographic parameters are presented in Figure S1 to illustrate the different oceanic regimes encountered along the transect and is the basis for dividing the study area into 5 regions/domains: Subpolar (> 50ºN), temperate (35ºN-50ºN), oligotrophic (20ºN-35ºN), riverine (10ºN-20ºN) and equatorial (0º-10ºN) (Figure 1, Table S1).

3.2 ^{234}Th:^{238}U disequilibrium and ^{234}Th fluxes

In general, ^{234}Th deficits were most apparent in the upper 100 m (Figure 2). Subpolar and temperate latitude stations (> 35ºN; PE2-PE16) however, tended to have deeper deficits and in some cases reached depths of 250 m. ^{234}Th activities in surface waters were typically < 1.5 dpm L^{-1}, although profiles from stations PE2, PE8 and PE11 showed equilibrium/slight deficits throughout the upper 100 m. Stations sampled to the south had reduced ^{234}Th deficits, such as PE22 and PE26 located in the subtropical gyre between 20ºN and 30ºN. ^{234}Th excesses were observable below ~200 m within

these subtropical latitudes, particularly at station PE24 (~26ºN), where [234]Th excess was observed throughout most of the upper water column.

In the riverine domain, moving towards the equator, [234]Th depletion became increasingly identifiable in the surface layers (< 100 m), although it was less intense than in the northern latitudes ([234]Th activities were > 2 dpm L^{-1}, except at stations PE31, PE32 and PE33, which were characterized by [234]Th activities of ~ 1.5 dpm L^{-1} in the upper 25 m). These stations also had lower [238]U activities in the upper 30 m relative to the other profiles (2.2-2.3 dpm L^{-1} compared to 2.5-2.6 dpm L^{-1}) due to low salinity in the surface layers. This suggests a significant riverine influence. In the equatorial domain, the deficit of [234]Th was smaller and shallower (at 100 m or above) than the deficits observed in the temperate latitudes. Station PE38 had [234]Th excesses between 100 and 200 m that extended to depths below 550 m, although the vertical resolution below 200 m was poor.

Th-234 fluxes were calculated at three depths (Figure S2): i) at 100 m, since that is the depth where *in situ* pumps were deployed, following historical sampling protocols; ii) to the base of the primary production zone (PPZ; defined as the depth where fluorescence is reduced to 10% of its maximum value, thus including the deep chlorophyll maximum layer; Owens et al., 2015), following a similar approach as the one proposed by Buesseler and Boyd (2009); and iii) to the shallowest depth where [234]Th and [238]U are equilibrium (deficit depth). Unfortunately, a PAR sensor was not deployed during the cruises; therefore we were unable to obtain an *in situ* estimate of the depth of the Z_{eu} during the cruise. However, the satellite-derived Z_{eu} show less depth variation than the depth horizons of the PPZ and the deficit depth, and is relatively close to the standardized depth horizon chosen of 100 m (Z_{eu} average depth 84 ± 14 m) (Table S1).

The three approaches were applied assuming a 1-dimensional steady-state model. Advection and diffusion processes are generally considered to be negligible relative to the downward flux of [234]Th, as assumed in the open ocean (see review by Savoye et al., 2006) and confirmed in previous studies in the North Atlantic (Buesseler et al., 2008; Resplandy et al., 2012; Thomalla et al., 2006).

However this assumption may fail in some of the more dynamic domains. For example, in the subpolar region the absence of stratification suggests strong vertical mixing (Figure S1). In the equatorial domain, upwelling may result in an underestimate of the [234]Th-derived carbon export estimates by as much as 25-35% (Buesseler et al., 1995). Thus the 1-dimensional steady-state model used here should be considered a lower limit.

Fluxes at 100 m were significantly different from those at the PPZ and the deficit depths (p = 0.047 and p = 0.036, respectively). Fluxes at the PPZ and the deficit depths were greater (by at least 10%) than those calculated at 100 m for the majority of the stations (18 stations, when using the PPZ, and 20 stations when estimating the flux at the deficit depth). [234]Th fluxes at the PPZ and the deficit depths were lower (> 10%) than those measured at 100 m at 9 and 2 stations, respectively, due to shallow [234]Th excess (Figure S2). Note that 3 stations did not have any shallow [234]Th deficits (PE22, PE24 and PE26, located between 23ºN and 30ºN). In the following discussion, we focus on the [234]Th fluxes at 100 m for easier comparison with prior studies. However, it is important to note that recent studies (Buesseler and Boyd, 2009) question the use of a fixed depth and highlight the importance of using a biologically meaningful depth to estimate [234]Th (and consequently C-derived) fluxes. Therefore, we also report the [234]Th fluxes at the PPZ and the deficit depths in Table S2.

Th-234 fluxes at 100 m ranged from -620 $\pm$ 180 dpm m^{-2} d^{-1} to 2740 $\pm$ 130 dpm m^{-2} d^{-1} (Table 1, Figure S2). The magnitude of the fluxes can be grouped by their latitudinal distributions: higher fluxes were found in the southern half of the temperate domain, and at a single station, PE6, in subpolar waters. Lower fluxes were measured in the subtropical gyre, particularly between ~20ºN and 30ºN, with negligible or even negative fluxes occurred at several stations (PE22, PE23, PE24, PE26 and PE27). The stations most influenced by the Amazon River plume (PE32 and PE33) had higher fluxes (> 1000 dpm m^{-2} d^{-1}) compared to those in the same region with no evidence of riverine influence, similarly to the fluxes observed in the southern part of the temperate domain Finally, the equatorial domain was the region where fluxes were less variable between stations, averaging 660 $\pm$ 170 dpm m^{-2} d^{-1} (Table 1, Figure S2).

3.3 C/^{234}Th ratios and derived C export fluxes

In situ pump deployments along the transect were limited due to time constraints. Measured C/^{234}Th ratios in large particles (> 53 μm) ranged from 2.3 to 16 μmol C dpm^{-1} (7.9 ± 5.0 μmol C dpm^{-1}; n = 11; Table 1). We used three different estimates of the C/^{234}Th ratio (Figure 3) in order to calculate C export fluxes for the entire section (Figure 4): i) using the average C/^{234}Th ratio obtained for each domain considering only the ratios from this study (ratios from Table 1; Figure 4 black circles), ii) following the approach of Owens et al. (2015), where C/^{234}Th ratios were derived from a power law regression (see Figure 8 from Owens et al., 2015) using the ratios from this study together with those from Owens et al., 2015 (see supplemental information for details; Figure 3A; Figure 4 white squares) and iii) using a compilation of the C/^{234}Th ratios found in the literature (including also the ratios from this study; ratios shown in Figure 3B; Figure 4 gray triangles).

Average C fluxes varied depending on the C/^{234}Th ratio used, ranging from 2.7 to 13 mmol C m^{-2} d^{-1} when applying the ratios from this study, from 1.2 to 12 mmol C m^{-2} d^{-1} when using the average ratios from the compilation of studies, and from 0.9 to 3.0 mmol C m^{-2} d^{-1} when using the power-law fit (Table 2). C fluxes obtained using the ratios from this study are not significantly different from those estimated using the compilation of C/^{234}Th ratios from the literature (p = 0.65), but they are significantly different from those obtained using the fitting curve (p = 0.0019). The C/^{234}Th ratios at 100 m measured in this study are considerably more variable than those measured by Owens et al. (2015) (Figure 3A). This is likely due in part to the timing of the cruises. Owens et al. (2015) obtained their samples in autumn/winter (October, November and December) and only south of 40ºN, whereas our cruises were conducted in spring/summer (May, June and July) when higher and more variable NPP occurs (Antoine et al., 1996). Given the biogeochemical variability along the transect, it would perhaps be more appropriate to obtain a power-law fit for each domain. Unfortunately, this is not possible due to the lack of measured C/^{234}Th ratio profiles. Therefore, this curve fit should be considered with caution since the differences between the ratios from both

studies and the larger amount of data from Owens et al. (2015) (with $C/^{234}Th$ ratios generally lower than the ratios from this study) may bias the curve (underestimate the $C/^{234}Th$ ratios).

Trends across latitudes within a given set of $C/^{234}Th$ ratios were observed, with lowest C fluxes found in the oligotrophic and equatorial domains (0.9 – 5.7 mmol C m^{-2} d^{-1}), followed by the temperate (3.0 – 7.3 mmol C m^{-2} d^{-1}), and riverine domains (2.4 – 12.2 mmol C m^{-2} d^{-1}) (Table 2). In the subpolar latitudes, there was large variability in C export (with deviations from the mean >100%), reflecting the high variability observed in ^{234}Th fluxes rather than $C/^{234}Th$ ratios per se.

3.4 Satellite-derived data: Particle Size Distribution and Net Primary Production

Particle size distribution derived from ocean color remote sensing data revealed spatial patterns that are consistent with the current understanding of oceanographic provinces (Figure S3), with the oligotrophic region characterized by lower particle abundances (indicated by high light transmission and low fluorescence and satellite-derived Chl-a data, Figure S1 and Figure 1) and larger quantities of picoplankton-sized particles. In contrast, microplankton-sized particles were more abundant in the temperate and subpolar areas, as well as in the riverine domain.

Satellite-derived NPP ranged from 0 to 70, from 13 to 260 and from 25 to 330 mmol C m^{-2} d^{-1} for the CbPM, VGPM and A&M96 models, respectively (Table S1). Highest values along the transect were obtained in the riverine and temperate domains for all the models, although the increase was much more apparent using the A&M96 model in the riverine and equatorial areas, while the VGPM model produced the highest NPP values in the temperate domain. If we do not consider the subpolar domain, for which the CbPM model provides a NPP of ~0 in three out of four stations, the lowest estimated NPP occurred in the oligotrophic domain, where the three models agree best. In the subpolar domain the A&M96 and VGPM models produce a similar amplitude of NPP values. The A&M96 and VGPM models were not significantly different (p = 0.15), whereas the CbPM was significantly different to the A&M96 (p = $5.2 \cdot 10^{-6}$) and to the VGPM (p = 0.0059) models, agreeing

with the intercomparison results reported by Carr et al. (2006). In general, the A&M96 and VGPM models generate 2-4 times higher NPP than CbPM, except in the equatorial domain.

4. DISCUSSION

Particle fluxes in the open ocean are strongly linked to surface productivity, plankton community structure and food web dynamics, which are in turn shaped by environmental conditions such as ocean physics and nutrient composition and supply (Ducklow et al., 2001). Given the observed regional differences in physical and ecological characteristics within the North Atlantic (Longhurst 1995, 2010) and the impact that distinct biome-specific scaling has on global organic carbon export predictions (Britten and Primeau, 2016), high spatial and temporal resolution has become essential for providing robust estimates of carbon export and to assess links and sensitivity to large scale ecosystem variability and global change (Galbraith et al., 2015; Honjo et al., 2014; Siegel et al., 2014). Here, we discuss estimates of ^{234}Th and C export fluxes considering the biogeochemical characteristics of the sampled areas and present C export efficiencies along the entire transect. Regional results are then placed in context of the entire North Atlantic and compared with previous studies (see Table S3 for references of the studies included in the compilation) and satellite-derived C export estimates.

4.1 ^{234}Th fluxes in the North Atlantic

There are a number of studies that have provided ^{234}Th fluxes (usually at 100 m) in the North Atlantic Ocean between 10°S and 64°N (see Figure 5 and Table S3 for locations and further details). Here we discuss our results in comparison with those prior studies (Figure S4). This compilation of studies is also used to compare the C export rates in each one of the domains (see section 4.2).

Subpolar (>50ºN)

Spring blooms may lead to substantial and efficient particle export in subpolar waters when

irradiance periods are longer and mixed layer depths are shallower (e.g., Martin et al., 2011). The sampling of this domain took place at the beginning of May, when the water column began to stratify, as indicated by shallow mixed layer depths (< 25 m; Table S1), favoring the beginning of the spring bloom. Satellite images showed an increase in surface Chl-a concentrations by the middle of April that continued during sampling (Figure S5). Silicate concentrations in the upper 50 m (Figure S1) were depleted, particularly at stations PE5 and PE6, suggesting that the bloom may have been dominated by siliceous phytoplankton, e.g., diatoms, consistent with the major phytoplankton group found in the region during the spring (Henson et al., 2006).

The subpolar region is an area with high seasonality, where production occurs in local spring blooms and where weather conditions (i.e., North Atlantic storm track) influence water column mixing. In such a dynamic region, phytoplankton blooms are patchy and the resulting variability in the magnitude of ^{234}Th export fluxes is expected. Indeed, we measured the largest ^{234}Th flux at 100 m at station PE6 (2740 ± 130 dpm m^{-2} d^{-1}), whereas the ^{234}Th flux at station PE8 was about an order of magnitude smaller (280 ± 180 dpm m^{-2} d^{-1}). Station PE8 was also characterized by ^{234}Th excess below 150 m, that was particularly marked at 250 m, which could indicate episodic export events prior to sampling that were subsequently remineralized.

Our estimates of ^{234}Th fluxes at PE5 and PE6 agree well with those reported by previous work in the same area during the same time frame (late spring) (Le Moigne et al., 2012; Moran et al., 2003; Sanders et al., 2010), although Le Moigne et al. (2012) measured two very high flux estimates (3950 and 4450 dpm m^{-2} d^{-1}). Larger variability in ^{234}Th fluxes was also observed in both our study and in Le Moigne et al. (2012) compared to Sanders et al. (2010) and Moran et al. (2003). This could be related to the strong negative phase of the North Atlantic Oscillation (NAO) in the winter of 2009-2010: Henson et al. (2013) showed that the extreme NAO influenced the wind conditions, favoring an unusually large phytoplankton bloom in the Irminger Sea at that time. In addition, the eruption of the Eyjafjallajökull Volcano in Iceland could have also enhanced the biological activity in the area by providing mineral enriched ash to this iron limited region, although the biological

response to ash-derived iron was shown to be relatively weak (Rogan et al., 2016).

Temperate (35ºN-50ºN)

Large phytoplankton blooms occur in the North Atlantic in spring, triggered by the increase in light and stratification of the water column (Henson et al., 2009; Sverdrup, 1953). As in the higher latitudes of this transect (> 50ºN), predominance of large phytoplankton, especially diatoms, is observed during blooms (e.g., Taylor et al., 1993). Indeed, diatom blooms in these high latitudes of the Atlantic Ocean can lead to significant particle export (Michaels and Silver, 1988), providing more than 50% of the annual biogenic particle mass flux in this region (Honjo and Manganini, 1993). Satellite images showed high Chl-a concentrations (> 7 mg m^{-3}) in those latitudes during the sampling period (Figure 1), where particle size distributions derived from satellite data also indicate the highest contribution of microplankton-sized particles (Figure S3). High fluorescence and beam attenuation coefficient values between 40ºN and 55ºN were also measured, with the highest values found at ~45ºN where stations PE12 and PE13 were sampled (Figure 2 and Figure S1). However, ^{234}Th fluxes at those stations were relatively low (~710 dpm m^{-2} d^{-1}), only ~ 20% of the ^{234}Th fluxes measured previously during blooms in this area (e.g., Buesseler et al., 1992), although they were within the range of fluxes measured previously (610 - 1330 dpm m^{-2} d^{-1}; Estapa et al., 2015; Le Moigne et al., 2013b; Owens et al., 2015; Thomalla et al., 2006). This might indicate that we sampled the northern zone at an early stage of the bloom, when significant nutrient drawdown had yet to occur. Indeed, satellite images showed low Chl-a concentrations (< 0.7 mg m^{-3}) at the beginning of May that subsequently reached a maximum (~10 mg m^{-3}) between 11th and 15th of May (Figure S5), when stations PE11, PE12 and PE13 were sampled and characterized by higher fluorescence concentrations relative to the rest of the stations of this domain (~2 mg m^{-3} *vs* < 0.5 mg m^{-3}; Figure 2). ^{234}Th fluxes at the southern stations (PE14, PE15 and PE16) were significantly higher (1350 - 1740 dpm m^{-2} d^{-1}), and we hypothesize that the bloom had already occurred by the time of sampling.

Oligotrophic (20ºN–35ºN)

Phytoplankton are nutrient-limited in the oligotrophic North Atlantic (Graziano et al., 1996; Mills et al., 2004) and blooms occur when the mixed layer reaches depths deep enough to supply nutrients to surface waters (January-March) (Steinberg et al., 2001). At low nutrient concentrations picophytoplankton groups, such as *Synechococcus* and *Prochlorococcus*, dominate (Lomas and Moran, 2011; Sarmiento and Gruber, 2006, and references therein; Steinberg et al., 2001), as also confirmed by the particle size distribution data (Figure S3).

The sampling of this region took place during the end of May and the middle/end of June. The mixed layers at the majority of the stations were < 20 m (Table S1), isolating the surface waters from the nutrient-rich deeper waters, and thus potentially limiting phytoplankton blooms. This is confirmed by the low satellite-derived Chl-a concentrations (Figure 1) and by the smaller (< 0.5 mg m^{-3}) and deeper (down to 135 m) fluorescence maxima compared to other regions (Table S1). Fluxes of ^{234}Th were low or negative from station PE21 (BATS; Bermuda Atlantic Time Series) to PE27, due to minor/negligible deficits of ^{234}Th or because remineralization in the upper 100 m compensated small ^{234}Th deficits. Previous works by Thomalla et al. (2006) and Owens et al., (2015) found similar results.

High surface concentrations of trace elements, Fe, Mn and Al (Middag et al., 2015; Rijkenberg et al., 2014) suggested that a dust event from the Sahara Desert may have occurred between 20ºN and 30ºN. Although phytoplankton can respond to such events (e.g. Cassar et al., 2007, Southern Ocean; Izquierdo et al., 2012, Mediterranean Sea; Mills et al., 2004 and Moore et al., 2006, North Atlantic Ocean), no phytoplankton bloom was observed during our study based on low beam attenuation, low fluorescence, and minimal ^{234}Th deficits (Figure S1 and Figure 2).

The ^{234}Th excess at depth at some stations, especially at station PE24, could be indicative of remineralization, suggesting that there might have been a phytoplankton response or particle export event in the past. Similar features were also reported by Sweeney et al. (2003) and Owens et al.

(2015). However, satellite images of Chl-a concentration (Figure S5) do not indicate the existence of a phytoplankton bloom prior to sampling nor do iron concentrations support remineralization (Rijkenberg et al., 2014). It is possible that ^{234}Th excess at depth is be due to the advection of ^{234}Th-rich adjacent waters (i.e. Kim et al., 2003), although there is no supporting evidence that this occurred.

Riverine (10ºN-20ºN)

Within the 10ºN - 20ºN domain the influence of the Amazon River plume in the surface waters was observed. Although the Amazon River estuary is located further south, within the equatorial domain, the riverine outflow was encountered between 11ºN and 18ºN, as evidenced by low salinity (< 34) in the upper 30 - 40 m and silicate concentrations reaching high as 8 μM at 10 m (Figure S1) (Reul et al., 2014; Rijkenberg et al., 2014). Fluorescence and beam attenuation also reflect the intrusion of the river plume as well as high satellite-derived Chl-a concentrations (Figure 1). Indeed, a significant change in color (greenish) and transparency of the waters was also visually evident from onboard. Riverine outflows enhance new primary production by providing nutrient inputs and by favoring the stratification of surface waters due to significant salinity gradients (Eppley and Peterson, 1979). DeMaster et al. (1986) showed that the high particle concentration within the Amazon River plume also scavenges particle-reactive species from open ocean waters. Stations in the core of the riverine input (i.e., PE32 and PE33) had larger ^{234}Th deficits, resulting in about two times higher ^{234}Th fluxes at 100 m than stations sampled outside the plume (average 1250 ± 320 vs 690 ± 220 dpm m^{-2} d^{-1}), and were comparable to ^{234}Th fluxes reported by Charette and Moran (1999) (1460 ± 80 dpm m^{-2} d^{-1}) and to those observed in the southern part of the temperate latitudes and in the northern limit of the oligotrophic region.

Equatorial region (0º-10ºN)

The influence of the Amazon River plume was also observed in the Equatorial region in the upper 25 m, especially at ~4ºN, with low salinities (< 34.5) and high silicate concentrations (~3.5 μM),

although the signal was weaker compared to the riverine domain and was not as evident in either fluorescence or beam attenuation values. The high nutrient concentrations were coincident with minimum oxygen concentrations and the entrance of the Antarctic Intermediate Water (AAIW) between 600 and 1200 m depth (van Aken, 2011).

Stations sampled within these latitudes had an average [234]Th flux at 100 m of 660 ± 170 dpm m^{-2} d^{-1}, similar to stations from the riverine domain, with the exception of those influenced by the Amazon River outflow. Previous studies in this region reported similar [234]Th flux estimates (Figure S4).

4.2 C export fluxes in the North Atlantic

There is a significant amount of data available regarding [234]Th-derived C fluxes in the North Atlantic. However, previous works have usually focused on the study of specific hydrographic or biological features (e.g., mesoscale eddies, phytoplankton blooms, etc.) that occur in relatively limited areas, or along transects with low spatial coverage (Figure 5 and Table S3). The GEOTRACES Program sections (this study and Owens et al., 2015) contribute significantly to the existing data set, providing greater spatial coverage for constraining C export. Indeed, combining our work with that of Owens et al. (2015) accounts for more than a 50% increase in the number of estimates presented in the global database of Le Moigne et al. (2013) from this area. These sections provide information that can be applied to not only develop better biogeochemical models of C export, but also the export and cycling of other trace elements, such as cobalt (Dulaquais et al., 2014). We also compiled ten previous studies that, when coupled with our work, amounts to a total of about 200 estimates of C export fluxes at 100-150 m (see Table S3) using the [234]Th-method in Atlantic open ocean waters (10ºS to 64ºN).

4.2.1 C/[234]Th ratios compilation

A critical component of the [234]Th-derived C fluxes is the C/[234]Th ratio measured in particulate

samples. This is necessary for converting [234]Th fluxes into C fluxes. Basic questions such as how to accurately sample the particles that are responsible for that export remain enigmatic and controversial (i.e., Lampitt et al., 2008; Burd et al., 2010; Bishop et al., 2012). Besides the technical difficulties in particle collection, the questions of how and why $C/^{234}$Th ratios vary in marine systems have been raised by several studies for more than a decade (see review by Buesseler et al., 2006), with still no clear agreement. Nonetheless, one of the most common methods is to use large particles (> 50 μm) collected using *in situ* filtration pumps placed below the depth of the Z_{eu} (usually standardized as 100-150 m), where $C/^{234}$Th variability is minimized and similar across techniques, e.g. sediment traps (e.g. Buesseler et al., 2008; Jacquet et al., 2011a; Maiti et al., 2008; Puigcorbé et al., 2015). The compilation presented here is based predominantly on ISP collected samples at 100 m, with the exception being the ratios obtained using sediment traps during the North Atlantic Bloom Experiment (NABE; Buesseler et al., 1992), and those from Charette and Moran (1999) that were measured in particles collected by filtering water (> 53 μm) from a rosette (Table S3).

$C/^{234}$Th ratios obtained using ISP at 100 m ranged from 2.3 to 16 μmolC dpm[-1], with no clear latitudinal pattern and were within the range observed from previous studies (0.9 – 25 μmolC dpm[-1]), although relatively high ratios were measured in the oligotrophic domain (up to 16 ± 2 μmolC dpm[-1]) where previous studies usually reported ratios < 5 μmolC dpm[-1] (Figure 3). This may be due in part to the relative timing of our sampling and the depth of the deep chlorophyll maximum (e.g., PE23). In fact, variability in the $C/^{234}$Th ratios from the compilation of studies, regardless of the domain, is highest in summer: May (2.3-25 μmol C dpm[-1]), July (2.5-22 μmol C dpm[-1]), and August (0.9-19 μmol C dpm[-1]). In winter months (October to January), $C/^{234}$Th ratios range from 2.2 to 6.7 μmol C dpm[-1] (data not shown).

Data on $C/^{234}$Th ratios are not evenly distributed across domains. A large fraction of the data correspond to the oligotrophic domain (n = 38), with the majority (n = 23) reported by Buesseler et

al. (2008) from a relatively small area (2º of latitude and ~5º of longitude) and focusing on mesoscale eddies. The subpolar domain is also highly sampled with regards to $C/^{234}Th$ ratios (n = 36) compared to the temperate (n = 23), riverine (n = 4), and equatorial domains (n = 4). Because of their proximity to the Mauritanian upwelling zone and their distance from the Amazon River outflow, stations between 5ºN and 20ºN in the eastern basin are considered as upwelling stations rather than riverine (Figure 5).

4.2.2 C export fluxes compilation

Three different estimates of $C/^{234}Th$ ratios in particles were applied to overcome the limited number of data collected along the transect and to obtain C export fluxes at 100 m at all the stations. Table 2 is a summary of the average C export rates for each domain, differentiating between this study and prior studies included in the comparison. When using the ratios from this study or those from the compilation of studies, the C export fluxes obtained were not significantly different (p = 0.65), whereas when applying the $C/^{234}Th$ ratio calculated using the power-law regression from Figure 3A, significantly lower estimates were obtained, particularly in the riverine and the subpolar domains (Table 2; Figure 4) (p = 0.0019). These low estimates are likely due to the fact that these domains were not included in the dataset from Owens et al. (2015) used to obtain the $C/^{234}Th$ fitting curve and also because ratios reported by Owens et al. (2015) were sampled during Octobert to December, when $C/^{234}Th$ ratios tend to be lower and less variable (see section 4.2.1 $C/^{234}Th$ ratios compilation). In contrast, the ratios obtained in this study and the compilation from previous studies were mainly obtained during spring/summer months.

Given that sampling was not evenly spaced through the months, nor through the domains, it is likely that seasonal and spatial biases exist in our compilation of $C/^{234}Th$ ratios. Nonetheless, while variability exists in $C/^{234}Th$ ratios even when sampled during the same period, this variability should be representative of the sampling period of that study. Therefore, in the next two sections we discuss export efficiencies and satellite-derived export models in comparison to [234]Th-derived C

export fluxes obtained using the average $C/^{234}Th$ ratio of this study based on the ISP samples at 100 m for each domain. This also further reduces uncertainties associated with differences in depth and allows for more direct comparisons with previous work that only focused on fluxes from 100 m.

Our dataset of C export fluxes at 100 m has a similar latitudinal trend in C export relative to previous studies (Figure 6). The emerging general picture is that highest C export fluxes (mmol C m^{-2} d^{-1}) are found in the subpolar domain (17 ± 12; $n = 38$), followed by the riverine (12 ± 12; $n = 8$), the temperate (8 ± 7; $n = 31$), the equatorial (4 ± 2; $n = 11$) and the oligotrophic (2 ± 2; $n = 98$) regions. High latitudes were characterized by high and variable C export fluxes (up to ~40 mmol C m^{-2} d^{-1}), likely due to the strong weather conditions (i.e., storms) and patchiness of phytoplankton blooms. The variability observed in the riverine region was also large, mainly due to the inclusion of stations clearly influenced by the Amazon outflow (stations PE32 and PE33 and also two stations from Charette and Moran, 1999), as well as stations located outside the river plume. The equatorial domain had among the lowest C flux estimates. The sole exception was one station reported by Thomalla et al. (2006) for which a C export of 25 ± 12 mmol C m^{-2} d^{-1} was attributed to the occurrence of a short phytoplankton bloom triggered by the nutrient input from a local upwelling event. The equatorial station from Charette and Moran (1999) (at 0.5ºS) also had a relatively high C flux export compared to the rest of the stations from the domain, although with large uncertainties. This large export flux was mainly driven by a high $C/^{234}Th$ ratio (20 µmol C dpm^{-1}), and the authors suggested that it was a consequence of dust inputs. However, the ratios from Charette and Moran (1999) were obtained from particles collected with a bottle rosette, which have been found to provide higher $C/^{234}Th$ ratios than *in situ* pumps (Liu et al., 2009).

4.3 Carbon export efficiencies

Ideally, export efficiencies should be estimated using the C export flux at either the base of the Z_{eu} or the PPZ (Buesseler and Boyd, 2009; Owens et al., 2015) rather than at a given depth horizon for all stations. However, due to the limitations of our dataset (e.g. no PAR sensor, limited vertical

resolution below 150 m, and modeled $C/^{234}Th$ ratios above and below 100 m) and in order to compare with prior studies, we focus on C export fluxes at 100 m.

Carbon export efficiencies (C export flux at 100 m/NPP) were determined using three different satellite-derived models for NPP estimates (see Table S1). Differences were found between the estimates of NPP, which were higher for most areas for A&M96 than for the other models, except for the temperate domain where the VGPM model produced consistently higher estimates. Despite the differences, the A&M96 and the VGPM models are not significantly different ($p = 0.15$) but they are different from the CbPM model ($p < 0.05$), which provided the lowest NPP values in most of the stations, except in the equatorial domain (Table S1). In general, the best agreement between the three models was found in the oligothropic area. Maiti et al. (2016) found similar results in the Gulf of Mexico, where the VGPM model resulted in about 40% higher NPP than the CbPM model. According to Westberry et al. (2008), the CbPM deviates significantly in the distribution and timing of production. Contrary to conventional "chlorophyll-based" models, which assign all changes in Chl-a to a change in biomass and hence a change in NPP, the CbPM distinguishes between changes in Chl-a caused by photo-adaptation versus changes due to growth (NPP). In addition, CbPM model deviations in the subpolar, temperate and riverine domains may also be related to the presence of coccolithophores and larger diatom sizes, which disproportionately increase backscattering due to their shells and frustules (Westberry et al., 2008).

Export efficiencies were generally < 25% across the entire transect when using the A&M96 and the VGPM models to derive NPP. When using the CbPM model, export efficiencies were significantly higher (up to 60%) in the transition stations between the oligotrophic and the temperate domains and at station PE32 (Figure 7). NPP from A&M96 lead to export efficiencies < 10% at the majority of stations (20 out of 33) and agrees well with the global compilation of direct estimates by Buesseler (1998). Unrealistically high export efficiencies (> 100%) were obtained at station PE6, in the subpolar domain, when using NPP derived from the VGPM model and at station PE16, in the temperate domain, when using NPP derived from the CbPM model (this model estimates 3-fold to

one order of magnitude lower NPP at PE16 relative to the surrounding stations). In the subpolar domain, export efficiencies obtained from the CbPM model are not presented due to unrealistically low NPP estimates.

Previous studies reported export efficiencies ranging between 2 and 42% in the eastern basin of the temperate domain (Buesseler et al., 1992; Le Moigne et al., 2013b). The average export efficiency in that domain for this study ranges from 5 to 18%, depending on the NPP model used and without considering station PE16 (Figure 7). In the oligotrophic domain, Buesseler et al. (2008) measured export efficiencies ranging from 2 to 12%. Our study calculates export efficiencies as high as 22% in the central part of the oligotrophic domain, although export efficiencies as high as 59% were estimated in the northern stations. Charette and Moran (1999) reported export efficiencies >100% at those stations affected by the Amazon River plume, but the highest value obtained in that area for this study was only 36% (using the VGPM model for NPP).

4.4 Comparison with satellite-based export models

Satellite-derived C export models have the potential to provide estimates of annual C export at regional to global scales. In addition, these models have a predictive power that can be used to forecast impacts on the global carbon cycle from possible changes in environmental conditions (e.g., changes in temperature, stratification, etc.). Satellite-based models, however, also have a myriad of assumptions and limitations and recent studies have highlighted the necessity to develop sub-ecosystem-scale parameterization in order to provide more accurate results (Galbraith et al., 2015; Siegel et al., 2014).

The three satellite-based export models described in section 2.3 (D05, L11 and H11) were applied and compared to the ^{234}Th-derived C export estimates obtained along the northern section of the GA02 transect. In order to apply these models, we used the three different satellite-derived NPP estimates from A&M96, CbPM and VGPM models (Table S1). About 85% of the C export fluxes derived from the ^{234}Th method were < 10 mmol C m^{-2} d^{-1}. Using this C export as a reference, we

observed that when using the NPP from the A&M96 model, the percentage of stations having fluxes below 10 mmol C m^{-2} d^{-1} was reduced to 46% and 55% (for D05 and L11 models, respectively) and to 58% (D05) and 73% (L11) when using the NPP from the VGPM model. In contrast, when using the NPP results from the CbPM model most of the stations (> 80%) had fluxes < 10 mmol C m^{-2} d^{-1} limit (Figure S6). Hence, the results of the export models were closer to our ^{234}Th-derived C export estimates when using the CbPM model. We therefore focus on the CbPM-derived NPP in the satellite-derived export models discussed below. The one exception is the subpolar region, where, because of unrealistically low NPP values, we used the average NPP obtained from the A&M96 and VGPM models.

Latitudinal C export fluxes derived from the three export models and ^{234}Th-derived C export are shown in Figure 8. The magnitude of the fluxes differs significantly between models and with ^{234}Th-derived C export. For example, H11 significantly underestimates C export along the entire section relative to ^{234}Th-derived C export estimates, whereas L11 and D05, despite the high variability, provide estimates that are in better agreement (within a 3-fold margin) (Figure 8). The export determined using the H11 model depends more heavily on temperature, and thus leads to low export fluxes (< 2 mmol C m^{-2} d^{-1}) throughout the entire section. Maiti et al. (2013) conducted a similar comparison between ^{234}Th- and satellite-derived C export in the Southern Ocean and observed a 2 to 4-fold overestimation of C export using the L11 and D05 models, with NPP obtained from the VGPM and the CbPM models. Stukel et al. (2015) found similar results in the eastern North Pacific Ocean. In the North Western Atlantic Ocean, we observe that D05 tends to significantly overestimate C export relative to *in situ* estimates in the equatorial domain, whereas L11 appears to underestimate C export, mainly in the northern half of the oligotrophic domain and at several riverine stations. Overall, the three models used here capture most of the geographical trends in C export, but not the absolute values. We therefore argue that parameterization of satellite-derived models should be revised and adapted to the specific oceanic regimes, taking into account factors beyond temperature and NPP, such as the trophic structure, grazing intensity or recycling

efficiency (Maiti et al., 2013). In addition already the variation among NPP model results shows that further optimization of these is necessary, which is an on-going process also fostered by various intercomparison and validation activities (e.g., Carr et al., 2006; Saba et al., 2011).

5. CONCLUSIONS

GEOTRACES is a global program whose objective is to "identify processes and quantify fluxes that control the distributions of key trace elements and isotopes in the ocean" (www.geotraces.org). The spatial coverage of ^{234}Th-derived C export presented here, together with the sections presented in Owens et al. (2015) increased significantly the number of C export estimates for the North Atlantic Ocean (i.e., Le Moigne et al., 2013a). Upper ocean ^{234}Th fluxes distribution agreed with previous studies, with high and variable export fluxes in the high latitudes and low to negligible fluxes in the oligotrophic region. ^{234}Th fluxes did not reflect the Sahara dust inputs between 20ºN and 30ºN identified by high concentrations of dissolved trace metals. On the other hand, the Amazon River outflow clearly impacted ^{234}Th inventories in the upper ocean, resulting in enhanced export to depth.

Carbon fluxes also compared well with previous studies, independently of the $C/^{234}$Th ratio estimate used, except for the riverine and subpolar domains where fluxes were underestimated when using the $C/^{234}$Th from the power-law curve. Due to differences between satellite-derived NPP estimates, the export efficiencies varied widely, however, the majority of stations had export efficiencies < 25% regardless of the NPP estimate used and were < 10% when using the A&M96 NPP estimates, which is in agreement with the results presented by Buesseler (1998) that indicate that the majority of the global ocean has export efficiencies < 10%.

When applying satellite-derived export models, similar latitudinal trends were observed between the three export models, although there were clear differences regarding the magnitude of the export. The Dunne et al. (2005) and Laws et al. (2011) models provided C export estimates closest to values obtained with the ^{234}Th approach (within a 3-fold difference), but with no clear trends

with regards to over or underestimating ^{234}Th-derived C export fluxes. The Henson et al. (2011) model, on the other hand, consistently provided lower export estimates, probably due to the stronger dependency on temperature. In general, satellite-based export models are strongly influenced by SST and NPP, but lack biological parameters that influence C export. Tuning models and including biological parameters at a regional scale will help improve satellite-modeling efforts and provide export estimates in better agreement with *in situ* observations. Continued observing efforts are needed to resolve these open questions and thereby reduce uncertainty in the global carbon budget and improve carbon cycle monitoring from satellite-based platforms.

Acknowledgements

References

Antoine, D., André, J.-M., Morel, A., 1996. Oceanic primary production: 2. Estimation at global scale from satellite (Coastal Zone Color Scanner) chlorophyll. Global Biogeochem. Cycles 10, 57–69. doi:10.1029/95GB02832

Antoine, D., Morel, A., 1996. Oceanic primary production: 1. Adaptation of a spectral light-photosynthesis model in view of application to satellite chlorophyll observations. Global Biogeochem. Cycles 10, 43–55. doi:10.1029/95GB02831

Behrenfeld, M.J., Boss, E., Siegel, D.A., Shea, D.M., 2005. Carbon-based ocean productivity and phytoplankton physiology from space. Global Biogeochem. Cycles 19, n/a–n/a. doi:10.1029/2004GB002299

Behrenfeld, M.J., Falkowski, P.G., 1997a. Photosynthetic rates derived from satellite-based chlorophyll concentration. Limnol. Oceanogr. 1–20. doi:10.4319/lo.1997.42.1.0001

Behrenfeld, M.J., Falkowski, P.G., 1997b. A consumer's guide to phytoplankton primary productivity models. Limnol. Oceanogr. 42, 1479–1491. doi:10.4319/lo.1997.42.7.1479

Bishop, J.K.B., Lam, P.J., Wood, T.J., 2012. Getting good particles: Accurate sampling of particles by large volume in-situ filtration. Limnol. Oceanogr. Methods 10, 681–710. doi:/10.4319/lom.2012.10.681

Brew, H.S., Moran, S.B., Lomas, M.W., Burd, A.B., 2009. Plankton community composition, organic carbon and thorium-234 particle size distributions, and particle export in the Sargasso Sea. J. Mar. Res. 67, 845–868. doi:10.1357/002224009792006124

Britten, G.L., Primeau, F.W., 2016. Biome-specific scaling of ocean productivity, temperature, and carbon export efficiency. Geophys. Res. Lett. 43, 5210–5216. doi:10.1002/2016GL068778

Buesseler, K.O., 1998. The decoupling of production and particulate export in the surface ocean. Global Biogeochem. Cycles 12, 297–310. doi:10.1029/97GB03366

Buesseler, K.O., Andrews, J.A., Hartman, M.C., Belastock, R., Chai, F., 1995. Regional estimates of the export flux of particulate organic carbon derived from thorium-234 during the JGOFS EqPac program. Deep Sea Res. Part II Top. Stud. Oceanogr. 42, 777–791. doi:10.1016/0967-0645(95)00043-P

Buesseler, K.O., Bacon, M.P., Kirk Cochran, J., Livingston, H.D., 1992. Carbon and nitrogen export during the JGOFS North Atlantic Bloom Experiment estimated from 234Th: 238U disequilibria. Deep Sea Res. Part A.Oceanographic Res. Pap. 39, 1115–1137. doi:10.1016/0198-0149(92)90060-7

Buesseler, K.O., Benitez-Nelson, C., Rutgers van der Loeff, M., Andrews, J., Ball, L., Crossin, G., Charette, M.A., 2001. An intercomparison of small-and large-volume techniques for thorium-234 in seawater. Mar. Chem. 74, 15–28.

Buesseler, K.O., Benitez-Nelson, C.R., Moran, S.B., Burd, A., Charette, M., Cochran, J.K., Coppola, L., Fisher, N.S., Fowler, S.W., Gardner, W.D., 2006. An assessment of particulate organic carbon to thorium-234 ratios in the ocean and their impact on the application of 234Th as a POC flux proxy. Mar. Chem. 100, 213–233. doi:10.1016/j.marchem.2005.10.013

Buesseler, K.O., Boyd, P.., 2009. Shedding light on processes that control particle export and flux attenuation in the twilight zone of the open ocean. Limnol. Oceanogr. 54, 1210–1232. doi:10.4319/lo.2009.54.4.1210

Buesseler, K.O., Lamborg, C., Cai, P., Escoube, R., Johnson, R., Pike, S., Masque, P., McGillicuddy, D., Verdeny, E., 2008. Particle fluxes associated with mesoscale eddies in the Sargasso Sea. Deep Sea Res. Part II Top. Stud. Oceanogr. 55, 1426–1444. doi:10.1016/j.dsr2.2008.02.007

Burd, A.B., Hansell, D. a., Steinberg, D.K., Anderson, T.R., Arístegui, J., Baltar, F., Beaupré, S.R., Buesseler, K.O., DeHairs, F., Jackson, G. a., Kadko, D.C., Koppelmann, R., Lampitt, R.S., Nagata, T., Reinthaler, T., Robinson, C., Robison, B.H., Tamburini, C., Tanaka, T., 2010. Assessing the apparent imbalance between geochemical and biochemical indicators of meso- and bathypelagic biological activity: What the @$♯! is wrong with present calculations of carbon budgets? Deep Sea Res. Part II Top. Stud. Oceanogr. 57, 1557–1571. doi:10.1016/j.dsr2.2010.02.022

Carr, M.-E., Friedrichs, M.A.M., Schmeltz, M., Aita, M.N., Antoine, D., Arrigo, K.R., Asanuma, I., Aumont, O., Barber, R., Behrenfeld, M., Bidigare, R., Buitenhuis, E.T., Campbell, J., Ciotti, A., Dierssen, H., Dowell, M., Dunne, J., Esaias, W., Gentili, B., Gregg, W., Groom, S., Hoepffner, N., Ishizaka, J., Kameda, T., Quéré, C. Le, Lohrenz, S., Marra, J., Mélin, F., Moore, K., Morel, A., Reddy, T.E., Ryan, J., Scardi, M., Smyth, T., Turpie, K., Tilstone, G., Waters, K., Yamanaka, Y., 2006. A comparison of global estimates of marine primary production from ocean color. Deep Sea Res. Part II Top. Stud. Oceanogr. 53, 741–770. doi:http://dx.doi.org/10.1016/j.dsr2.2006.01.028

Casacuberta, N., Christl, M., Lachner, J., van der Loeff, M., Masque, P., Synal, H.-A., 2014. A first transect of 236 U in

the North Atlantic Ocean. Geochim. Cosmochim. Acta 133, 34–46. doi:10.1016/j.gca.2014.02.012

Cassar, N., Bender, M.L., Barnett, B.A., Fan, S., Moxim, W.J., Levy, H., Tilbrook, B., 2007. The Southern Ocean biological response to aeolian iron deposition. Science (80-.). 317, 1067–1070. doi:10.1126/science.1144602

Charette, M.A., Moran, S.B., 1999. Rates of particle scavenging and particulate organic carbon export estimated using 234Th as a tracer in the subtropical and equatorial Atlantic Ocean. Deep. Res. Part II 46, 885–906. doi:10.1016/S0967-0645(99)00006-5

Coale, K.H., Bruland, K.W., 1985. 234Th:238U disequilibria within the California Current. Limnol. Oceanogr. 30, 22–33. doi:10.4319/lo.1985.30.1.0022

Cochran, J.K., Masqué, P., 2003. Short-lived U/Th series radionuclides in the ocean: tracers for scavenging rates, export fluxes and particle dynamics. Rev. Mineral. Geochemistry 52, 461–492. doi:10.2113/0520461

DeMaster, D.J., Kuehl, S.A., Nittrouer, C.A., 1986. Effects of suspended sediments on geochemical processes near the mouth of the Amazon River: examination of biological silica uptake and the fate of particle-reactive elements. Cont. Shelf Res. 6, 107–125. doi:http://dx.doi.org/10.1016/0278-4343(86)90056-7

Ducklow, H.W., Steinberg, D.K., Buesseler, K.O., 2001. Upper ocean carbon export and the biological pump. Oceanogr. DC-OCEANOGRAPHY Soc. 14, 50–58.

Dulaquais, G., Boye, M., Middag, R., Owens, S., Puigcorbé, V., Buesseler, K., Masqué, P., de Baar, H., Carton, X., 2014. Contrasting biogeochemical cycles of cobalt in the surface Western Atlantic Ocean. Global Biogeochem. Cycles 2014GB004903. doi:10.1002/2014GB004903

Dunne, J.P., Armstrong, R.A., Gnanadesikan, A., Sarmiento, J.L., 2005. Empirical and mechanistic models for the particle export ratio. Global Biogeochem. Cycles 19, GB4026. doi:10.1029/2004GB002390

Eppley, R.W., 1972. Temperature and phytoplankton growth in the sea. Fish. Bull. 70, 1063–1085.

Eppley, R.W., Peterson, B.J., 1979. Particulate organic matter flux and planktonic new production in the deep ocean. Nature 282, 677–680.

Estapa, M.L., Siegel, D.A., Buesseler, K.O., Stanley, R.H.R., Lomas, M.W., Nelson, N.B., 2015. Decoupling of net community and export production on submesoscales in the Sargasso Sea. Global Biogeochem. Cycles 29, 1266–1282. doi:10.1002/2014GB004913

Galbraith, E.D., Dunne, J.P., Gnanadesikan, A., Slater, R.D., Sarmiento, J.L., Dufour, C.O., Souza, G.F. de, Bianchi, D., Claret, M., Rodgers, K.B., Marvasti, S.S., 2015. Complex functionality with minimal computation: Promise and pitfalls of reduced- tracer ocean biogeochemistry models. J. Adv. Model. Earth Syst. 7, 2012–2028. doi:10.1002/2015MS000463

Gerringa, L.J.A., 2010. Geotraces West Atlantic leg 1. Cruise report 64PE319 on RV Pelagia.

GlobColour, 2015. GlobColour User Guide; REF GC-UM_ACR-PUG-01. Version 3.1 [WWW Document]. URL http://www.globcolour.info/CDR_Docs/GlobCOLOUR_PUG.pdf (accessed 2.13.15).

Grasshoff, K., Ehrhardt, M., Kremling, K., 1983. Methods of Seawater Analysis, 2nd ed. Verlag Chemie GmbH, Weinheim.

Graziano, L.M., Geider, R.J., Li, W.K.W., Olaizola, M., 1996. Nitrogen limitation of North Atlantic phytoplankton: Analysis of physiological condition in nutrient enrichment experiments. Aquat. Microb. Ecol. 11, 53–64. doi:10.3354/ame011053

Gustafsson, Ö., Gschwend, P.M., Buesseler, K.O., 1997a. Using 234Th disequilibria to estimate the vertical removal rates of polycyclic aromatic hydrocarbons from the surface ocean. Mar. Chem. 57, 11–23. doi:http://dx.doi.org/10.1016/S0304-4203(97)00011-X

Gustafsson, Ö., Gschwend, P.M., Buesseler, K.O., 1997b. Settling removal rates of PCBs into the northwestern Atlantic derived from 238U-234Th disequilibria. Environ. Sci. Technol. 31, 3544–3550. doi:10.1021/es970299u

Henson, S.A., Dunne, J.P., Sarmiento, J.L., 2009. Decadal variability in North Atlantic phytoplankton blooms. J. Geophys. Res. Ocean. 114. doi:10.1029/2008JC005139

Henson, S.A., Painter, S.C., Penny Holliday, N., Stinchcombe, M.C., Giering, S.L.C., 2013. Unusual subpolar North Atlantic phytoplankton bloom in 2010: Volcanic fertilization or North Atlantic Oscillation? J. Geophys. Res. Ocean. 118, 4771–4780. doi:10.1002/jgrc.20363

Henson, S.A., Sanders, R., Holeton, C., Allen, J.T., 2006. Timing of nutrient depletion, diatom dominance and a lower-boundary estimate of export production for Irminger Basin, North Atlantic. Mar. Ecol. Prog. Ser. 313, 73–84. doi:10.3354/meps313073

Henson, S.A., Sanders, R., Madsen, E., Morris, P.J., Le Moigne, F., Quartly, G.D., 2011. A reduced estimate of the strength of the ocean's biological carbon pump. Geophys. Res. Lett. 38, L04606. doi:10.1029/2011GL046735

Honjo, S., Eglinton, T.I., Taylor, C.D., Ulmer, K.M., Sievert, S.M., Bracher, A., German, C.R., Edgcomb, V., Francois, R., Inglesias-Rodriguez, M.D., others, 2014. Understanding the role of the Biological Pump in the Global Carbon Cycle: An imperative for Ocean Science. Oceanography 27, 10–16. doi:10.5670/oceanog.2014.78

Honjo, S., Manganini, S.J., 1993. Annual biogenic particle fluxes to the interior of the North Atlantic Ocean; studied at 34°N 21°W and 48°N 21°W. Deep Sea Res. Part II Top. Stud. Oceanogr. 40, 587–607. doi:http://dx.doi.org/10.1016/0967-0645(93)90034-K

Honjo, S., Manganini, S.J., Krishfield, R.A., Francois, R., 2008. Particulate organic carbon fluxes to the ocean interior and factors controlling the biological pump: A synthesis of global sediment trap programs since 1983. Prog. Oceanogr. 76, 217–285. doi:10.1016/j.pocean.2007.11.003

Izquierdo, R., Benítez-Nelson, C.R., Masqué, P., Castillo, S., Alastuey, A., Àvila, A., 2012. Atmospheric phosphorus deposition in a near-coastal rural site in the NE Iberian Peninsula and its role in marine productivity. Atmos. Environ. 49, 361–370. doi:10.1016/j.atmosenv.2011.11.007

Jacquet, S.H.M., Dehairs, F., Dumont, I., Becquevort, S., Cavagna, A.-J., Cardinal, D., 2011. Twilight zone organic carbon remineralization in the Polar Front Zone and Subantarctic Zone south of Tasmania. Deep Sea Res. Part II Top. Stud. Oceanogr. 58, 2222–2234. doi:/10.1016/j.dsr2.2011.05.029

Kahru, M., 2017. Ocean productivity from space: Commentary. Global Biogeochem. Cycles 31, 214–216. doi:10.1002/2016GB005582

Kim, G., Hussain, N., Church, T.M., 2003. Tracing the advection of organic carbon into the subsurface Sargasso Sea using a 228Ra/226Ra tracer. Geophys. Res. Lett. 30. doi:10.1029/2003GL017565

Knap, A.H., Michaels, A., Close, A.R., Ducklow, H., Dickson, A.G., 1996. Protocols for the joint global ocean flux study (JGOFS) core measurements. JGOFS, Repr. IOC Manuals Guid. No. 29, UNESCO 1994 19, 1–210.

Lampitt, R.S., Boorman, B., Brown, L., Lucas, M., Salter, I., Sanders, R., Saw, K., Seeyave, S., Thomalla, S.J., Turnewitsch, R., 2008. Particle export from the euphotic zone: Estimates using a novel drifting sediment trap, 234Th and new production. Deep Sea Res. Part I Oceanogr. Res. Pap. 55, 1484–1502. doi:10.1016/j.dsr.2008.07.002

Laws, E.A., D'Sa, E., Naik, P., 2011. Simple equations to estimate ratios of new or export production to total production from satellite-derived estimates of sea surface temperature and primary production. Limnol. Oceanogr. Methods 9, 593–601. doi:10.4319/lom.2011.9.593

Le Moigne, F.A.C., Henson, S.A., Sanders, R.J., Madsen, E., 2013a. Global database of surface ocean particulate organic carbon export fluxes diagnosed from the 234Th technique. Earth Syst. Sci. Data 5, 295–304. doi:10.5194/essd-5-295-2013

Le Moigne, F.A.C., Sanders, R.J., Villa-Alfageme, M., Martin, A.P., Pabortsava, K., Planquette, H., Morris, P.J., Thomalla, S.J., 2012. On the proportion of ballast versus non-ballast associated carbon export in the surface ocean. Geophys. Res. Lett. 39, L15610. doi:10.1029/2012GL052980

Le Moigne, F.A.C., Villa-Alfageme, M., Sanders, R.J., Marsay, C., Henson, S., García-Tenorio, R., 2013b. Export of organic carbon and biominerals derived from< sup> 234</sup> Th and< sup> 210</sup> Po at the Porcupine Abyssal Plain. Deep Sea Res. Part I Oceanogr. Res. Pap. 72, 88–101.

Liu, Z., Cochran, J.K., Lee, C., Gasser, B., Miquel, J.C., Wakeham, S.G., 2009. Further investigations on why POC concentrations differ in samples collected by Niskin bottle and in situ pump. Deep Sea Res. Part II Top. Stud. Oceanogr. 56, 1558–1567. doi:10.1016/j.dsr2.2008.12.019

Lomas, M.W., Moran, S.B., 2011. Evidence for aggregation and export of cyanobacteria and nano-eukaryotes from the Sargasso Sea euphotic zone. Biogeosciences 8, 203–216. doi:10.5194/bg-8-203-2011

Longhurst, A., 1995. Seasonal cycles of pelagic production and consumption. Prog. Oceanogr. 36, 77–167. doi:http://dx.doi.org/10.1016/0079-6611(95)00015-1

Longhurst, A.R., 2010. Ecological geography of the sea, 2nd ed. Academic Press.

Maiti, K., Benitez-Nelson, C.R., Buesseler, K.O., 2010. Insights into particle formation and remineralization using the short-lived radionuclide, Thoruim-234. Geophys. Res. Lett. 37, L15608. doi:10.1029/2010GL044063

Maiti, K., Benitez-Nelson, C.R., Rii, Y., Bidigare, R., 2008. The influence of a mature cyclonic eddy on particle export in the lee of Hawaii. Deep Sea Res. Part II Top. Stud. Oceanogr. 55, 1445–1460.

Maiti, K., Bosu, S., D'Sa, E.J., Adhikari, P.L., Sutor, M., Longnecker, K., 2016. Export fluxes in northern Gulf of

Mexico - Comparative evaluation of direct, indirect and satellite-based estimates. Mar. Chem. 184, 60–77. doi:http://dx.doi.org/10.1016/j.marchem.2016.06.001

Maiti, K., Buesseler, K.O., Pike, S.M., Benitez-Nelson, C., Cai, P., Chen, W., Cochran, K., Dai, M., Dehairs, F., Gasser, B., Kelly, R.P., Masqué, P., Miller, L.A., Miquel, J.C., Moran, S.B., Morris, P.J., Peine, F., Planchon, F., Renfro, A.A., Rutgers van der Loeff, M., Santschi, P.H., Turnewitsch, R., Waples, J.T., Xu, C., 2012. Intercalibration studies of short-lived Thorium-234 in the water column and marine particles. Limnol. Ocean. Methods 10, 631–644. doi:10.4319/lom.2012.10.631

Maiti, K., Charette, M.A., Buesseler, K.O., Kahru, M., 2013. An inverse relationship between production and export efficiency in the Southern Ocean. Geophys. Res. Lett. 40, 1557–1561. doi:doi:10.1002/grl.50219

Martin, P., Lampitt, R.S., Jane Perry, M., Sanders, R., Lee, C., D'Asaro, E., 2011. Export and mesopelagic particle flux during a North Atlantic spring diatom bloom. Deep Sea Res. Part I Oceanogr. Res. Pap. 58, 338–349. doi:10.1016/j.dsr.2011.01.006

Mawji, E., Schlitzer, R., Masferrer, E., Abadie, C., Abouchami, W., Anderson, R.F., Baars, O., Bakker, K., Baskaran, M., Bates, N.R., Bluhm, K., Bowie, A., Bown, J., Boye, M., Boyle, E.A., Branekkec, P., Bruland, K.W., Brzezinski, M.A., Bucciarelli, E., Buesseler, K., Butler, E., Cai, P., Cardinal, D., Casciotti, K., Chaves, J., Cheng, H., Chever, F., Church, T.M., Colman, A.S., Conway, T.M., Croot, P.L., Cutter, G.A., de Baar, H.J.W., de Souza, G.F., Dehairs, F., Deng, F., Thi Dieu, H., Dulaquais, G., Echegoyen-Sanz, Y., Edwards, R.L., Fahrbach, E., Fitzsimmons, J., Fleisher, M., Frank, M., Friedrich, J., Fripiat, F., Galer, S.J.G., Gamo, T., Garcia-Solsona, E., Gerringa, L.J.A., Godoy, J.M., Gonzalez, S., Grossteffan, E., Hatta, M., Hayes, C.T., Heller, M.I., Henderson, G., Huang, K.-F., Jeandel, C., Jenkins, W.J., John, S., Kenna, T.C., Klunder, M., Kretschmer, S., Kumamoto, Y., Laan, P., Labatut, M., Lacan, F., Lam, P.J., Lannuzel, D., Le Moigne, F., Lechtenfeld, O., Lohan, M.C., Lu, Y., Masqué, P., McClain, C.R., Measures, C., Middag, R., Moffett, J., Navidad, A., Nishioka, J., Noble, A., Obata, H., Ohnemus, D.C., Owens, S., Planchon, F., Pradoux, C., Puigcorbé, V., Quay, P., Radic, A., Rehkämper, M., Remenyi, T., Rijkenberg, M.J.A., Rintoul, S., Robinson, L.F., Roeske, T., Rosenberg, M., Rutgers van der Loeff, M., Ryabenko, E., Saito, M.A., Roshan, S., Salt, L., Sarthou, G., Schauer, U., Scott, P., Sedwick, P.N., Sha, L., Shiller, A.M., Sigman, D.M., Smethie, W., Smith, G.J., Sohrin, Y., Speich, S., Stichel, T., Stutsman, J., Swift, J.H., Tagliabue, A., Thomas, A., Tsunogai, U., Twining, B.S., van Aken, H.M., van Heuven, S., van Ooijen, J., van Weerlee, E., Venchiarutti, C., Voelker, A.H.L., Wake, B., Warner, M.J., Woodward, E.M.S., Wu, J., Wyatt, N., Yoshikawa, H., Zheng, X.-Y., Xue, Z., Zieringer, M., Zimmer, L.A., 2015. The GEOTRACES Intermediate Data Product 2014. Mar. Chem. 1–8. doi:http://dx.doi.org/10.1016/j.marchem.2015.04.005

Michaels, A.F., Silver, M.W., 1988. Primary production, sinking fluxes and the microbial food web. Deep Sea Res. Part A.Oceanographic Res. Pap. 35, 473–490. doi:10.1016/0198-0149(88)90126-4

Middag, R., van Hulten, M.M.P., Van Aken, H.M., Rijkenberg, M.J.A., Gerringa, L.J.A., Laan, P., de Baar, H.J.W., 2015. Dissolved aluminium in the ocean conveyor of the West Atlantic Ocean: Effects of the biological cycle, scavenging, sediment resuspension and hydrography. Mar. Chem. 177, 69–86. doi:10.1016/j.marchem.2015.02.015

Mills, M.M., Ridame, C., Davey, M., La Roche, J., Geider, R.J., 2004. Iron and phosphorus co-limit nitrogen fixation in the eastern tropical North Atlantic. Nature 429, 292–294. doi:10.1038/nature02550

Moore, C.M., Mills, M.M., Milne, A., Langlois, R., Achterberg, E.P., Lochte, K., Geider, R.J., La Roche, J., 2006. Iron limits primary productivity during spring bloom development in the central North Atlantic. Glob. Chang. Biol. 12, 626–634. doi:10.1111/j.1365-2486.2006.01122.x

Moran, S.B., Weinstein, S.E., Edmonds, H.N., Smith, J.N., Kelly, R.P., Pilson, M.E.Q., Harrison, W.G., 2003. Does 234Th/238U disequilibrium provide an accurate record of the export flux of particulate organic carbon from the upper ocean? Limnol. Oceanogr. 48, 1018–1029. doi:10.4319/lo.2003.48.3.1018

Morel, A., 1991. Light and marine photosynthesis: a spectral model with geochemical and climatological implications. Prog. Oceanogr. 26, 263–306.

Morel, A., Antoine, D., Babin, M., Dandonneau, Y., 1996. Measured and modeled primary production in the northeast Atlantic (EUMELI JGOFS program): the impact of natural variations in photosynthetic parameters on model predictive skill. Deep Sea Res. Part I Oceanogr. Res. Pap. 43, 1273–1304. doi:http://dx.doi.org/10.1016/0967-0637(96)00059-3

Morel, A., Berthon, J.-F., 1989. Surface pigments, algal biomass profiles, and potential production of the euphotic layer: Relationships reinvestigated in view of remote-sensing applications. Limnol. Oceanogr. 34, 1545–1562. doi:10.4319/lo.1989.34.8.1545

Owens, S.A., Buesseler, K.O., Sims, K.W.W., 2011. Re-evaluating the 238U-salinity relationship in seawater: Implications for the 238U-234Th disequilibrium method. Mar. Chem. 127, 31–39. doi:10.1016/j.marchem.2011.07.005

Owens, S.A., Pike, S., Buesseler, K.O., 2015. Thorium-234 as a tracer of particle dynamics and upper ocean export in the Atlantic Ocean. Deep Sea Res. Part II Top. Stud. Oceanogr. 116, 42–59. doi:http://dx.doi.org/10.1016/j.dsr2.2014.11.010

Palevsky, H.I., Quay, P.D., Nicholson, D.P., 2016. Discrepant estimates of primary and export production from satellite algorithms, a biogeochemical model, and geochemical tracer measurements in the North Pacific Ocean. Geophys. Res. Lett. 43, 8645–8653. doi:10.1002/2016GL070226

Pike, S.M., Buesseler, K.O., Andrews, J., Savoye, N., 2005. Quantification of Th-234 recovery in small volume seawater samples by inductively coupled plasma-mass spectrometry.   . J. Radioanal. Nucl. Chem. 263, 355–360.

Puigcorbé, V., Benitez- Nelson, C.R., Masqué, P., Verdeny, E., White, A.E., Popp, B.N., Prahl, F.G., Lam, P.J., 2015. Small phytoplankton drive high summertime carbon and nutrient export in the Gulf of California and Eastern Tropical North Pacific. Global Biogeochem. Cycles 29, 1309–1332. doi:10.1002/ 2015GB005134

Puigcorbé, V., Roca-Martí, M., Masqué, P., Benitez-Nelson, C.R., Rutgers v. d. Loeff, M., Laglera, L.M., Bracher, A., Cheah, W., Strass, V.H., Hoppema, M., Santos-Echeandía, J., Hunt, B.P. V, Pakhomov, E.A., Klaas, C., 2017. Particulate organic carbon export across the Antarctic Circumpolar Current at 10°E: Differences between north and south of the Antarctic Polar Front. Deep Sea Res. Part II Top. Stud. Oceanogr. 138, 86–101. doi:https://doi.org/10.1016/j.dsr2.2016.05.016

Resplandy, L., Martin, A.P., Le Moigne, F., Martin, P., Aquilina, A., Mémery, L., Lévy, M., Sanders, R., 2012. How does dynamical spatial variability impact 234Th-derived estimates of organic export? Deep Sea Res. Part I Oceanogr. Res. Pap. 68, 24–45. doi:http://dx.doi.org/10.1016/j.dsr.2012.05.015

Reul, N., Fournier, S., Boutin, J., Hernandez, O., Maes, C., Chapron, B., Alory, G., Quilfen, Y., Tenerelli, J., Morisset, S., Kerr, Y., Mecklenburg, S., Delwart, S., 2014. Sea Surface Salinity Observations from Space with the SMOS Satellite: A New Means to Monitor the Marine Branch of the Water Cycle. Surv. Geophys. 35, 681–722. doi:10.1007/s10712-013-9244-0

Rijkenberg, M., 2010. Geotraces West Atlantic leg 2. Cruise report 64PE321 on RV Pelagia.

Rijkenberg, M.J.A., Middag, R., Laan, P., Gerringa, L.J.A., van Aken, H.M., Schoemann, V., de Jong, J.T.M., de Baar, H.J.W., 2014. The Distribution of Dissolved Iron in the West Atlantic Ocean. PLoS One 9, e101323. doi:10.1371/journal.pone.0101323

Rogan, N., Achterberg, E.P., Le Moigne, F.A.C., Marsay, C.M., Tagliabue, A., Williams, R.G., 2016. Volcanic ash as an oceanic iron source and sink. Geophys. Res. Lett. 43, 2732–2740. doi:10.1002/2016GL067905

Saba, V.S., Friedrichs, M.A.M., Antoine, D., Armstrong, R.A., Asanuma, I., Behrenfeld, M.J., Ciotti, A.M., Dowell, M., Hoepffner, N., Hyde, K.J.W., Ishizaka, J., Kameda, T., Marra, J., Mélin, F., Morel, A., O'Reilly, J., Scardi, M., Smith Jr., W.O., Smyth, T.J., Tang, S., Uitz, J., Waters, K., Westberry, T.K., 2011. An evaluation of ocean color model estimates of marine primary productivity in coastal and pelagic regions across the globe. Biogeosciences 8, 489–503. doi:10.5194/bg-8-489-2011

Sanders, R., Morris, P.J., Poulton, A.J., Stinchcombe, M.C., Charalampopoulou, A., Lucas, M.I., Thomalla, S.J., 2010. Does a ballast effect occur in the surface ocean? Geophys. Res. Lett. 37, L08602. doi:10.1029/2010GL042574

Sarmiento, J.L., Gruber, N., 2006. Ocean biogeochemical dynamics. Cambridge Univ Press.

Savoye, N., Benitez-Nelson, C., Burd, A.B., Cochran, J.K., Charette, M., Buesseler, K.O., Jackson, G.A., Roy-Barman, M., Schmidt, S., Elskens, M., 2006. 234Th sorption and export models in the water column: a review. Mar. Chem. 100, 234–249. doi:10.1016/j.marchem.2005.10.014

Savoye, N., Buesseler, K.O., Cardinal, D., Dehairs, F., 2004. 234Th deficit and excess in the Southern Ocean during spring 2001: Particle export and remineralization. Geophys.Res.Lett 31, L12301. doi:10.1029/2004GL019744

Siegel, D.A., Buesseler, K.O., Behrenfeld, M.J., Benitez-Nelson, C.R., Boss, E., Brzezinski, M.A., Burd, A., Carlson, C.A., D'Asaro, E.A., Doney, S.C., Perry, M.J., Stanley, R.H.R., Steinberg, D.K., 2016. Prediction of the Export and Fate of Global Ocean Net Primary Production: The EXPORTS Science Plan. Front. Mar. Sci. 3. doi:10.3389/fmars.2016.00022

Siegel, D.A., Buesseler, K.O., Doney, S.C., Sailley, S.F., Behrenfeld, M.J., Boyd, P.W., 2014. Global assessment of ocean carbon export by combining satellite observations and food-web models. Global Biogeochem. Cycles 28, 181–196. doi:10.1002/2013GB004743

Steinberg, D.K., Carlson, C.A., Bates, N.R., Johnson, R.J., Michaels, A.F., Knap, A.H., 2001. Overview of the US JGOFS Bermuda Atlantic Time-series Study (BATS): a decade-scale look at ocean biology and biogeochemistry. Deep Sea Res. Part II Top. Stud. Oceanogr. 48, 1405–1447. doi:10.1016/S0967-0645(00)00148-X

Stukel, M.R., Kahru, M., Benitez-Nelson, C.R., Décima, M., Goericke, R., Landry, M.R., Ohman, M.D., 2015. Using Lagrangian-based process studies to test satellite algorithms of vertical carbon flux in the eastern North Pacific Ocean. J. Geophys. Res. Ocean. 120, 7208–7222. doi:10.1002/2015JC011264

Sverdrup, H.U., 1953. On conditions for the vernal blooming of phytoplankton. ICES J. Mar. Sci. 18, 287. doi:10.1093/icesjms/18.3.287

Sweeney, E.N., McGillicuddy, D.J., Buesseler, K.O., 2003. Biogeochemical impacts due to mesoscale eddy activity in the Sargasso Sea as measured at the Bermuda Atlantic Time-series Study (BATS). Deep Sea Res. Part II Top. Stud. Oceanogr. 50, 3017–3039. doi:10.1016/j.dsr2.2003.07.008

Taylor, A.H., Harbour, D.S., Harris, R.P., Burkill, P.H., Edwards, E.S., 1993. Seasonal succession in the pelagic ecosystem of the North Atlantic and the utilization of nitrogen. J. Plankton Res. 15, 875–891. doi:10.1093/plankt/15.8.875

Thomalla, S.J., Turnewitsch, R., Lucas, M., Poulton, A., 2006. Particulate organic carbon export from the North and South Atlantic gyres: The 234Th/238U disequilibrium approach. Deep Sea Res. Part II Top. Stud. Oceanogr. 53, 1629–1648. doi:10.1016/j.dsr2.2006.05.018

van Aken, H., 2011. GEOTRACES, the hydrography of the Western Atlantic Ocean.

Volk, T., Hoffert, M.I., 1985. Ocean Carbon Pumps: Analysis of Relative Strengths and Efficiencies in Ocean-Driven Atmospheric CO2 Changes, in: The Carbon Cycle and Atmospheric CO2: Natural Variations Archean to Present. American Geophysical Union, pp. 99–110. doi:10.1029/GM032p0099

Waples, J.T., Benitez-Nelson, C., Savoye, N., Rutgers van der Loeff, M., Baskaran, M., Gustafsson, Ö., 2006. An introduction to the application and future use of 234Th in aquatic systems. Mar. Chem. 100, 166–189. doi:10.1016/j.marchem.2005.10.011

Weinstein, S.E., Moran, S.B., 2005. Vertical flux of particulate Al, Fe, Pb, and Ba from the upper ocean estimated from 234Th/238U disequilibria. Deep Sea Res. Part I Oceanogr. Res. Pap. 52, 1477–1488. doi:http://dx.doi.org/10.1016/j.dsr.2005.03.008

Westberry, T., Behrenfeld, M.J., Siegel, D.A., Boss, E., 2008. Carbon-based primary productivity modeling with vertically resolved photoacclimation. Global Biogeochem. Cycles 22, GB2024. doi:10.1029/2007GB003078

Figure captions and Tables manuscript DSRI 2832

Figure 1: Stations locations along the northern GA02 transect, between May 2nd and July 4th 2010, overlain by mean chlorophyll-a concentration (mg m^{-3}) derived from MODIS AQUA remote sensing data (http://oceancolor.gsfc.nasa.gov) corresponding to sampling time (i.e., May for subpolar and temperate domains, May-June for oligotrophic domain, June for riverine domain and June-July for equatorial domain). White symbols correspond to stations sampled during the 64PE319 cruise and black symbols during the 64PE321 cruise. Stars indicate those stations where particle samples were also collected. Black horizontal dashed lines indicate the different domains sampled.

Figure 2: Concentration profiles for ^{234}Th (in dpm L^{-1}; black diamonds and solid line), ^{238}U (in dpm L^{-1}; dotted line) and fluorescence (in mg m^{-3}; green line) of each station.

Figure 3: Panel A shows the $C/^{234}$Th ratios profiles from large particles from Owens et al. (2015) for the North Atlantic cruise GA03 (circles), together with the $C/^{234}$Th ratios obtained during this study (triangles), with symbols color coded by domain. The power law regression presented in panel A was derived within the depth ranges of the PPZ and the depth of the ^{234}Th deficits using 20-40 m-binned averages (black diamonds) (see Supplemental Information for details). This regression can be used to calculate $C/^{234}$Th ratios at a desired depth (e.g., PPZ or deficit depth in Table S2). Panel B presents the box plots by domain for the $C/^{234}$Th ratios from a compilation of studies conducted in the North Atlantic Ocean (see Table S3 for details).

Figure 4: Carbon export fluxes at 100 m estimated using different $C/^{234}$Th ratios: using the domain average from ratios obtained during this study (black circles), using the domain average from a compilation of previous works together with data from this study (gray triangles, see Table S3 for a description of the studies used) and using the ratios derived from the power-law regression shown in Figure 3A (white squares).

Figure 5: Map with the locations considered in the compilation for each study. Dashed lines indicate the limits of the domains. Two stations from Charette and Moran (1999) marked with * should be considered riverine rather than equatorial since they were affected by the Amazon outflow.

Figure 6: Carbon export fluxes at 100-150 m for this study (red symbols) and for the compilation of studies (gray symbols). The different symbols are used to indicate the sampling time. Two stations marked with * should be considered riverine rather than equatorial because they were affected by the Amazon outflow (Charette and Moran, 1999). Data from the compilation of studies located between 10ºN-20ºN were sampled in the eastern basin, therefore they belong to the upwelling domain rather than the riverine.

Figure 7: Export efficiencies obatined using three different NPP estimates (see Table S1) and compared to carbon export fluxes at 100 m calculated using the $C/^{234}$Th ratios measured during this study.

Figure 8: Upper panel: Satellite-derived export models comparison (using NPP estimated with the CbPM model, except for the subpolar domain where the NPP values were averaged between A&M96 and the VGPM model; see text for details), together with ^{234}Th-derived C export fluxes obtained at 100 m using $C/^{234}$Th from this study averaged by domains. Lower panel: Ratios between the three satellite-based export models *vs* ^{234}Th-derived export fluxes. The shaded gray area represents a 3-fold difference between estimates.

Table 1: ^{234}Th fluxes, $C/^{234}$Th ratios and C fluxes at 100 m.

Cruise	Domain	Station	^{234}Th flux at 100m	$C/^{234}$Th from this study	C flux using $C/^{234}$Th ratios from this study

Cruise	Domain	#	dpm m^{-2} d^{-1}	μmol C dpm^{-1}	mmol C m^{-2} d^{-1}
64PE319	Subpolar	PE2	320 ± 190	4.692 ± 0.064	1.48 ± 0.89
		PE5	1040 ± 160	*7.6 ± 7.1*	*7.8 ± 7.5*
		PE6	2740 ± 130	15.68 ± 0.22	43.0 ± 2.1
		PE8	280 ± 180	2.323 ± 0.015	0.66 ± 0.41
		PE11	470 ± 180	8.02 ± 0.16	3.7 ± 1.4
	Temperate	PE12	710 ± 170	*6.7 ± 1.9*	*4.7 ± 1.8*
		PE13	710 ± 180	5.306 ± 0.064	3.79 ± 0.95
		PE14	1350 ± 200	*6.7 ± 1.9*	*9.0 ± 2.9*
		PE15	1740 ± 170	*6.7 ± 1.9*	*11.6 ± 3.5*
		PE16	1650 ± 170	*6.7 ± 1.9*	*11.0 ± 3.3*
		PE17	1170 ± 180	*10.2 ± 5.4*	*11.9 ± 6.6*
		PE18	1270 ± 180	*10.2 ± 5.4*	*13.0 ± 7.1*
		PE19	720 ± 200	*10.2 ± 5.4*	*7.3 ± 4.4*
64PE321	Oligotrophic	PE21	610 ± 160	9.47 ± 0.56	5.8 ± 1.6
		PE22	-250 ± 210	*10.2 ± 5.4*	*-2.6 ± -2.5*
		PE23	77 ± 200	16.1 ± 1.9	1.2 ± 3.3
		PE24	-620 ± 180	*10.2 ± 5.4*	*-6.3 ± -3.8*
		PE25	320 ± 160	*10.2 ± 5.4*	*3.3 ± 2.4*
		PE26	-310 ± 180	5.231 ± 0.081	-1.63 ± -0.92
		PE27	140 ± 190	*10.2 ± 5.4*	*1.4 ± 2.0*
		PE28	510 ± 160	*10.2 ± 5.4*	*5.3 ± 3.2*
		PE29	930 ± 110	*7.5 ± 7.3*	*7.0 ± 6.8*
		PE30	490 ± 220	12.56 ± 0.86	6.2 ± 2.8
	Riverine	PE31	670 ± 150	*7.5 ± 7.3*	*5.0 ± 5.0*
		PE32	1020 ± 160	*7.5 ± 7.3*	*7.7 ± 7.5*
		PE33	1480 ± 140	2.344 ± 0.057	3.46 ± 0.34
		PE34	670 ± 160	*7.5 ± 7.3*	*5.0 ± 5.0*
	Equatorial	PE35	800 ± 170	*4.14 ± 0.11*	*3.28 ± 0.69*
		PE36	830 ± 110	4.14 ± 0.11	3.39 ± 0.45
		PE37	630 ± 140	*4.14 ± 0.11*	*2.56 ± 0.57*
		PE38	680 ± 130	*4.14 ± 0.11*	*2.78 ± 0.54*
		PE39	640 ± 130	*4.14 ± 0.11*	*2.61 ± 0.54*
		PE40	360 ± 150	*4.14 ± 0.11*	*1.48 ± 0.60*

Note: C/^{234}Th ratios in italic are the averaged value per domain. C export fluxes in italic are obatined using the averaged ratios.

Table 2: Summary of C fluxes in the North Atlantic. For this study, three different C flux estimates are reported depending on the C/^{234}Th ratio used.

			This study			Other studies	
			C flux at 100 m				**C flux at 100 or 150 m**
	Lat	**n**	C/^{234}Th ratios from this study	C/^{234}Th ratios from compilation	C/^{234}Th from fitting curve	**n**	
			mmol C m^{-2} d^{-1}				mmol C m^{-2} d^{-1}
Subpolar	50ºN-65ºN	5	13 ± 20	11 ± 12	3.0 ± 3.2	33[a, b, c]	17.5 ± 9.6
Temperate	35ºN-50ºN	6	7.3 ± 3.6	6.0 ± 3.0	3.0 ± 1.5	25[d,e,f,g]	8.3 ± 8.3
Oligotrophic	20ºN-35ºN	11	3.5 ± 5.9	1.2 ± 2.2	0.9 ± 1.6	87[d,e,h,i]	2.3 ± 1.6
Riverine	10ºN-20ºN	6	5.7 ± 1.5	12.2 ± 4.9	2.4 ± 1.0	2[j]	30 ± 12
Equatorial	0º-10ºN	6	2.7 ± 0.7	5.7 ± 1.5	1.8 ± 0.5	5[d,e,i]	4.9 ± 2.0

[a] Le Moigne et al. (2012)
[b] Sanders et al. (2010)
[c] Moran et al. (2003)
[d] Owens et al. (2015)
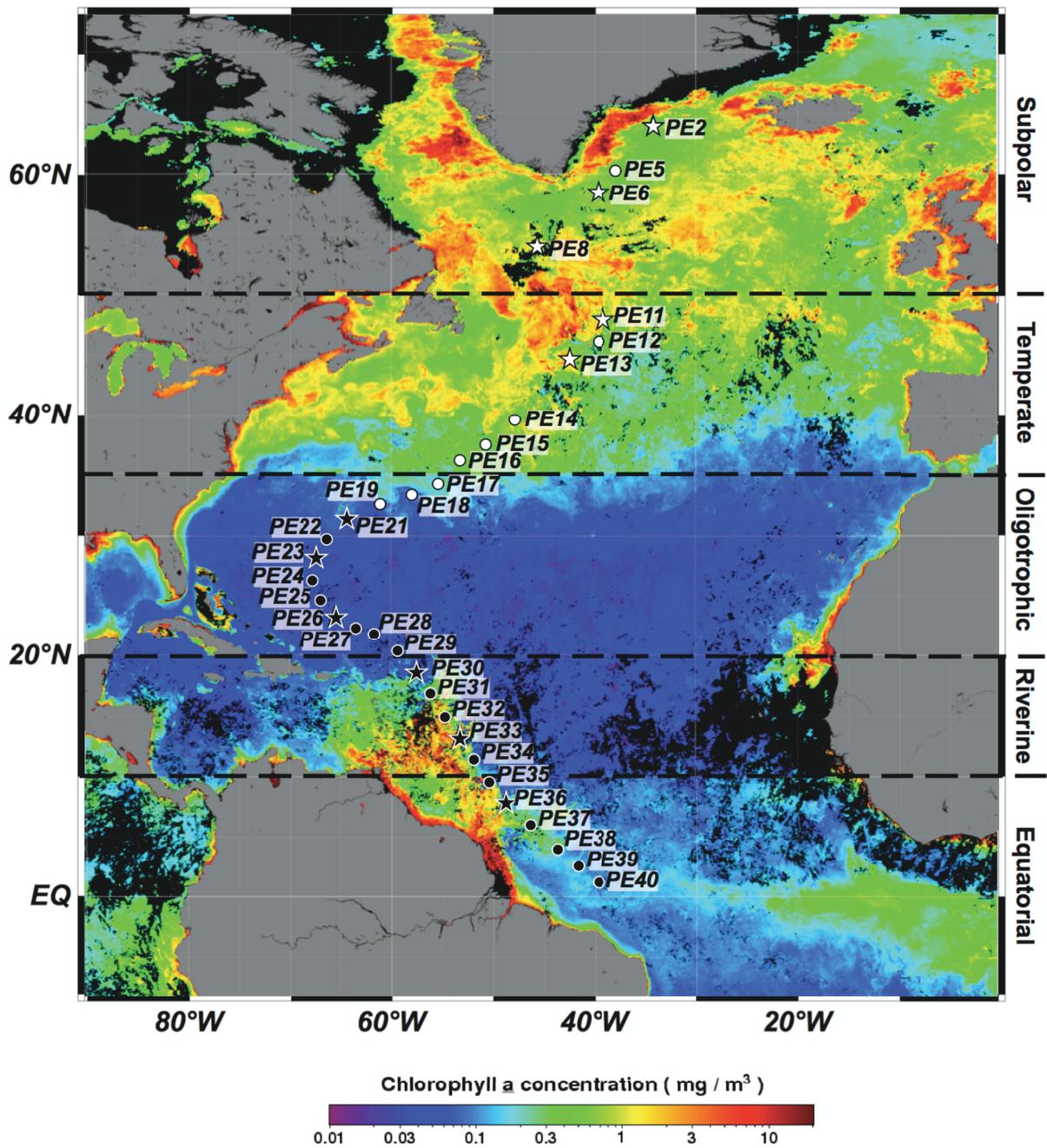[e] Thomalla et al. (2006)
[f] Le Moigne et al. (2013)
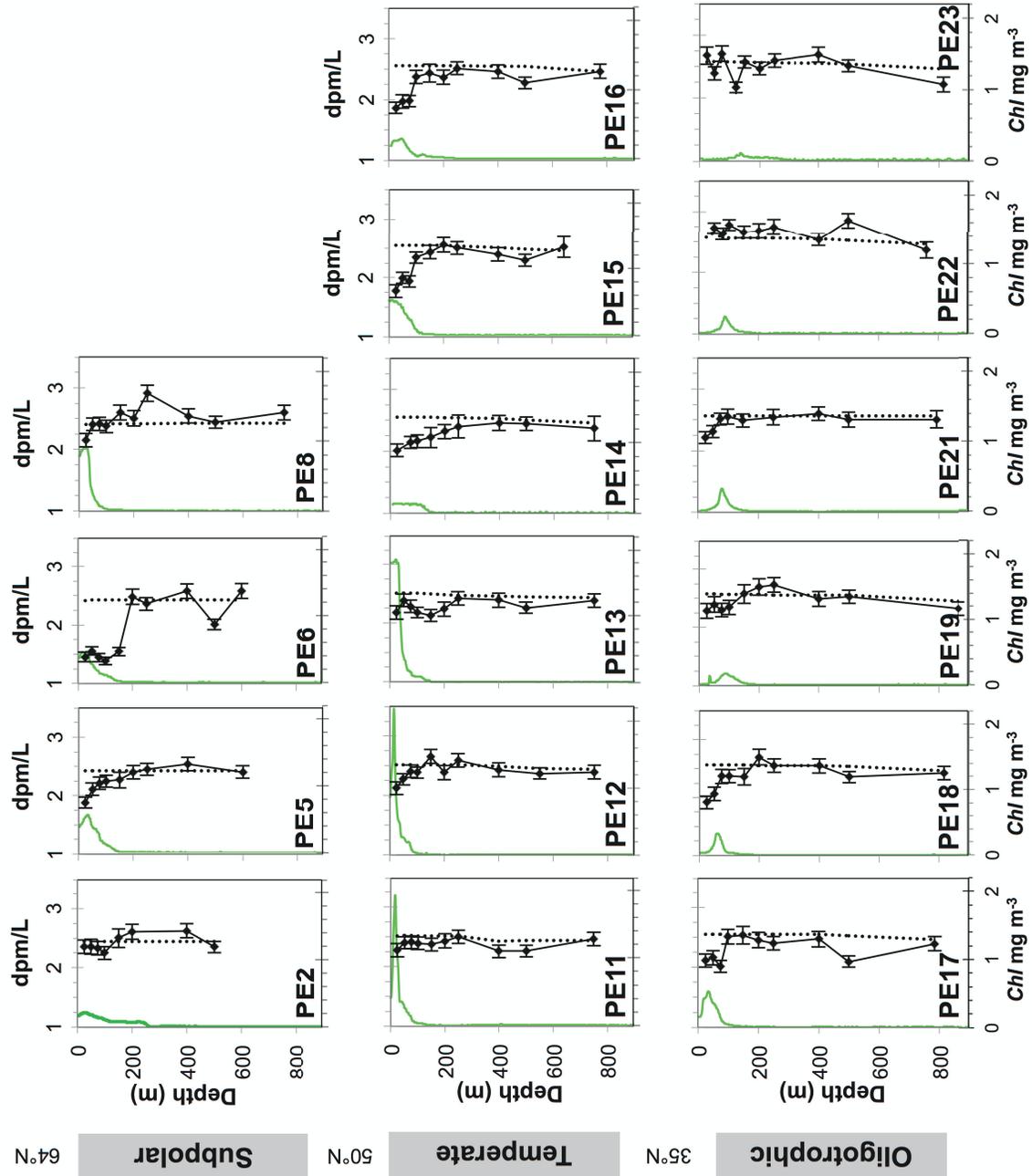[g] Buesseler et al. (1992)
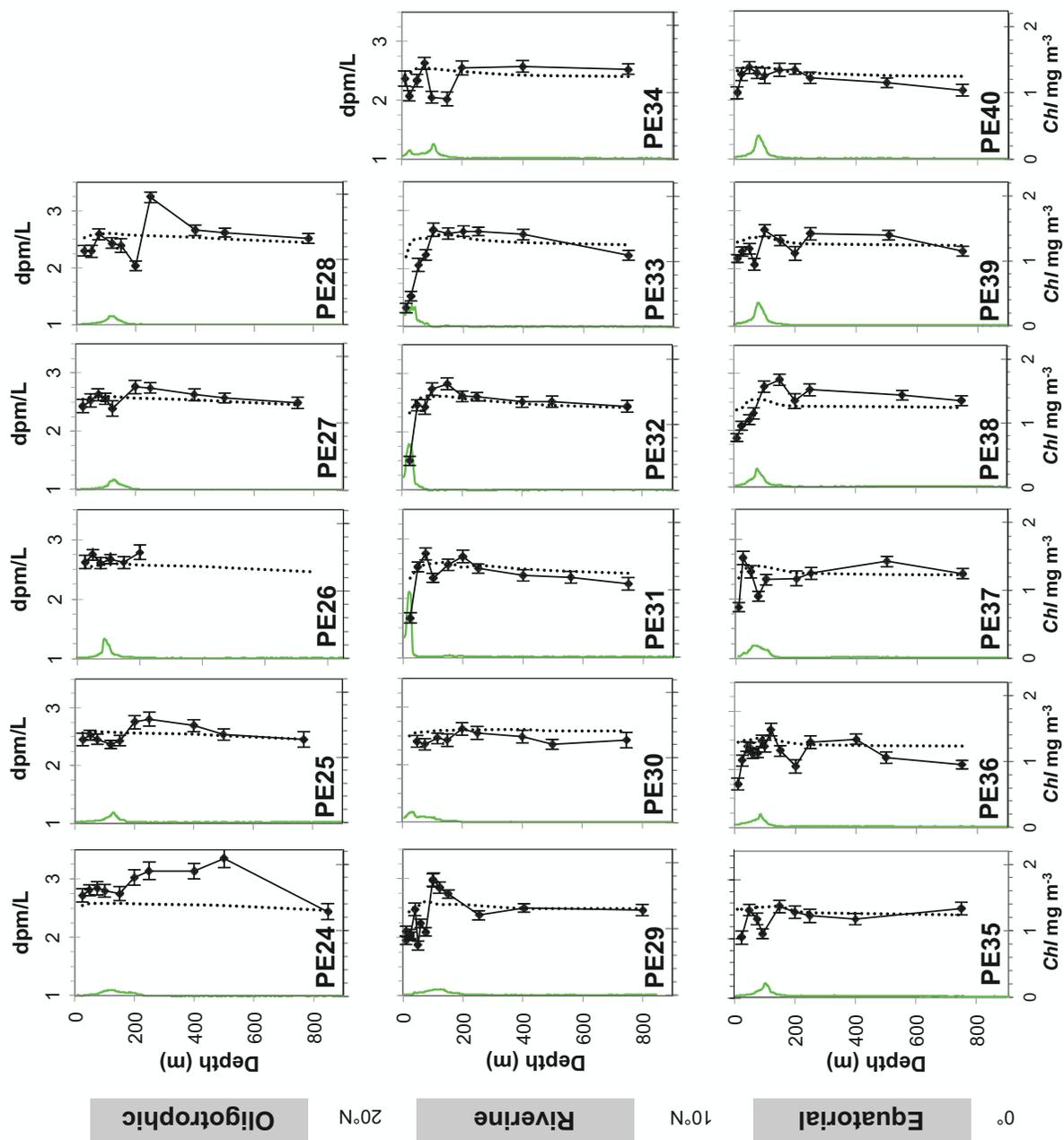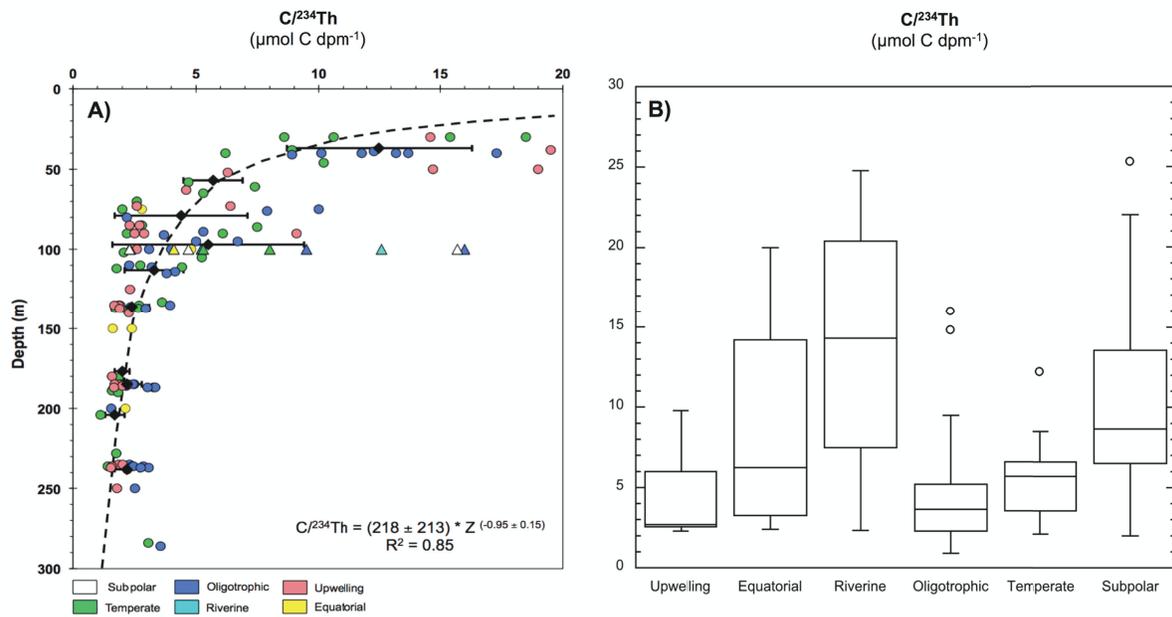[h] Buesseler et al. (2008)
[i] Brew et al. (2009)

[j] Charette and Moran (1999). Note that two of the stations were considered riverine rather than equatorial because they were affected by the Amazon outflow.
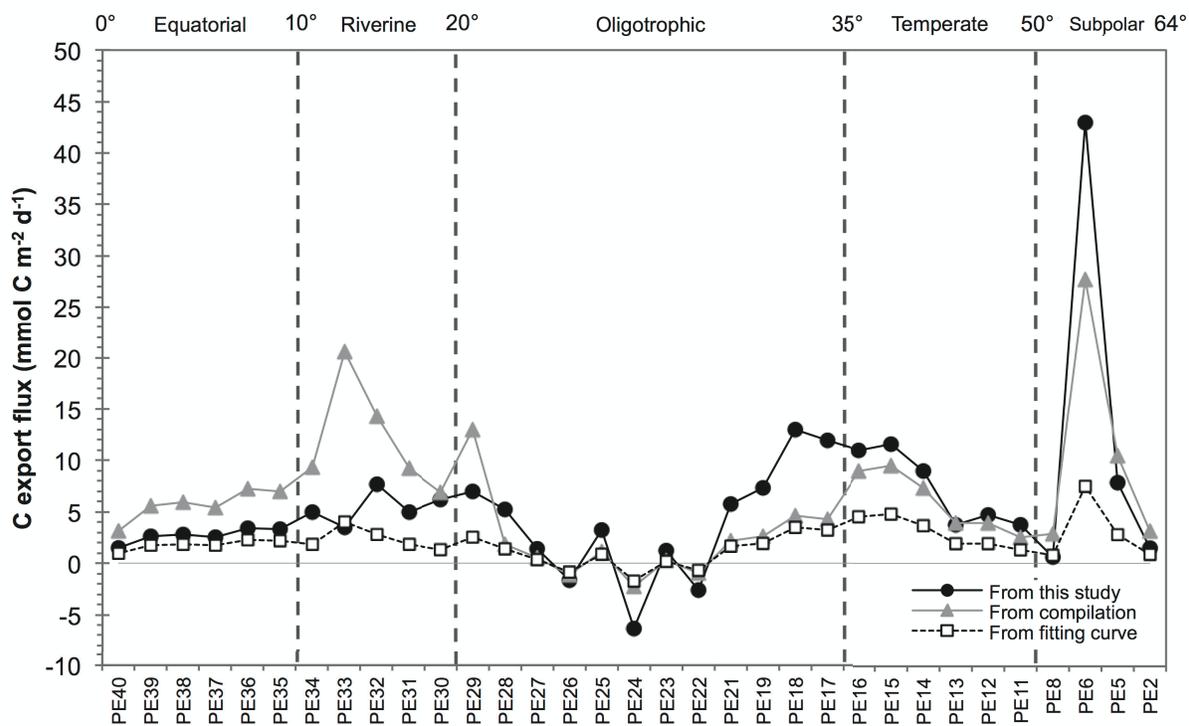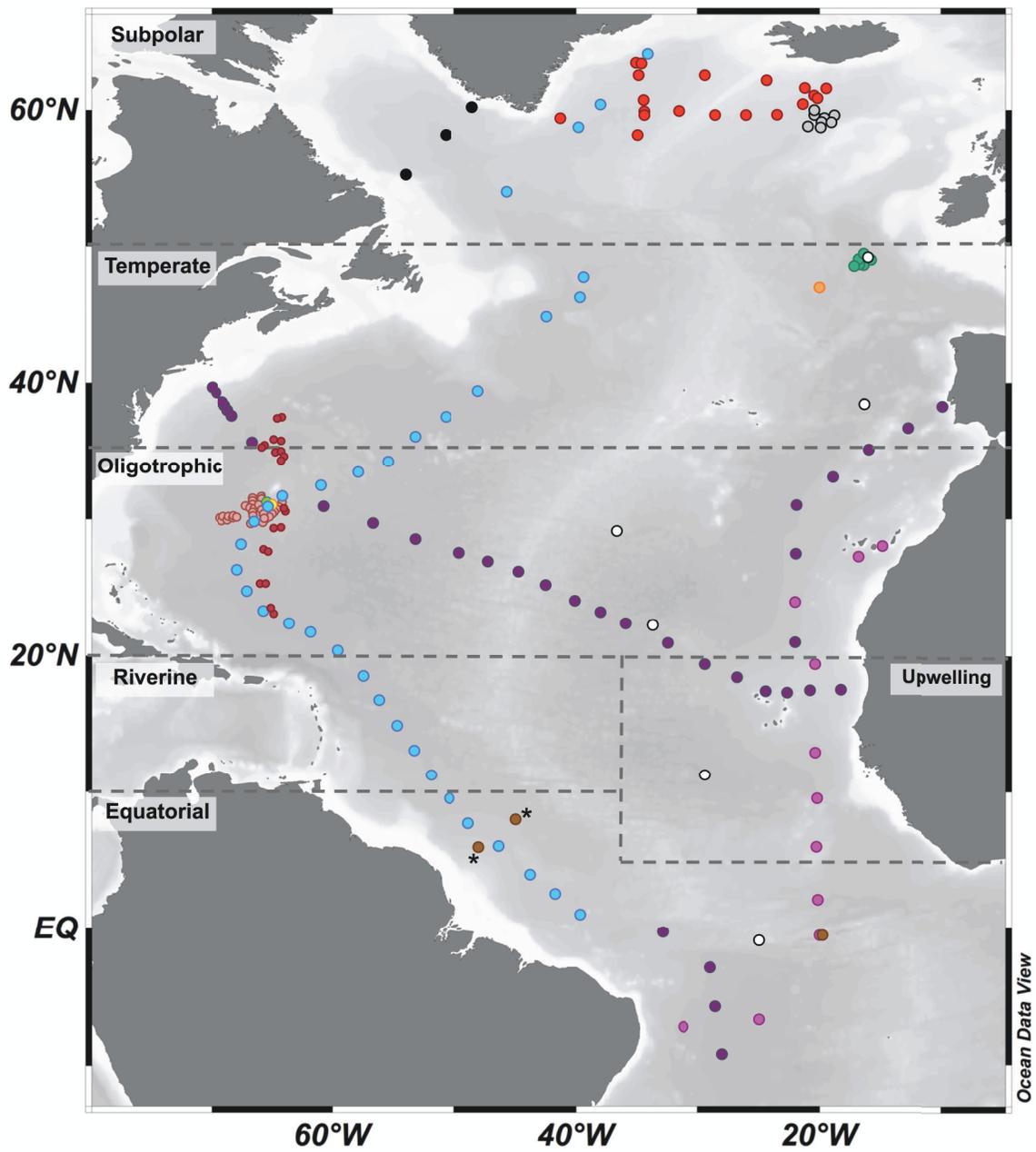
Chlorophyll _a_ concentration (mg / m^3)

C/²³⁴Th
(µmol C dpm⁻¹)

A)

$$C/^{234}Th = (218 \pm 213) * Z^{(-0.95 \pm 0.15)}$$
$$R^2 = 0.85$$

Depth (m)

Subpolar Oligotrophic Upwelling
Temperate Riverine Equatorial

C/²³⁴Th
(µmol C dpm⁻¹)

B)

Upwelling Equatorial Riverine Oligotrophic Temperate Subpolar

Ocean Data View

C flux (mmol C m⁻² d⁻¹) plotted against latitude from -10°S to 60°N, divided into regions: Equatorial, Riverine, Oligotrophic, Temperate, and Subpolar. Legend: X February, + March-April, ◇ May, ○ June, △ July, □ August, ✕ Oct-Nov-Dec.